Key Points:
- Global warming ranges from 1 to 4.5°C by 2100
- Atlantic overturning circulation decreases by 2100
- There is a collapse of the overturning in RCP8.5 in E2-R models

Correspondence to:
L. Nazarenko,
larissa.s.nazarenko@nasa.gov

Future climate change under RCP emission scenarios with GISS ModelE2

L. Nazarenko[1,2], G. A. Schmidt[2], R. L. Miller[2], N. Tausnev[2,3], M. Kelley[2,3], R. Ruedy[2,3], G. L. Russell[2], I. Aleinov[1,2], M. Bauer[2,4], S. Bauer[1,2], R. Bleck[1,4], V. Canuto[1], Y. Cheng[1,2], T. L. Clune[5], A. D. Del Genio[2], G. Faluvegi[1,2], J. E. Hansen[2,6], R. J. Healy[1,2], N. Y. Kiang[2], D. Koch[1,7], A. A. Lacis[2], A. N. LeGrande[2], J. Lerner[1,2], K. K. Lo[2,3], S. Menon[8], V. Oinas[2,3], J. Perlwitz[2,4], M. J. Puma[1,2], D. Rind[2], A. Romanou[2,4], M. Sato[1,2,6], D. T. Shindell[1], S. Sun[2,3], K. Tsigaridis[1,2], N. Unger[9], A. Voulgarakis[1,2,10], M.-S. Yao[1,3], and Jinlun Zhang[11]

[1]Center for Climate Systems Research, Columbia University, New York, New York, USA, [2]NASA Goddard Institute for Space Studies, New York, New York, USA, [3]Trinnovim LLC, New York, New York, USA, [4]Department of Applied Physics and Applied Mathematics, Columbia University, New York, New York, USA, [5]NASA Goddard Space Flight Center, Greenbelt, Maryland, USA, [6]Now at Earth Institute, Columbia University, New York, New York, USA, [7]Now at Department of Energy, Washington, District of Columbia, USA, [8]Lawrence Berkeley National Laboratory, Berkeley, California, USA, [9]Yale University, New Haven, Connecticut, USA, [10]Department of Physics, Imperial College, London, UK, [11]University of Washington, Seattle, Washington, USA

Abstract We examine the anthropogenically forced climate response for the 21st century representative concentration pathway (RCP) emission scenarios and their extensions for the period 2101–2500. The experiments were performed with ModelE2, a new version of the NASA Goddard Institute for Space Sciences (GISS) coupled general circulation model that includes three different versions for the atmospheric composition components: a noninteractive version (NINT) with prescribed composition and a tuned aerosol indirect effect (AIE), the TCAD version with fully interactive aerosols, whole-atmosphere chemistry, and the tuned AIE, and the TCADI version which further includes a parameterized first indirect aerosol effect on clouds. Each atmospheric version is coupled to two different ocean general circulation models: the Russell ocean model (GISS-E2-R) and HYCOM (GISS-E2-H). By 2100, global mean warming in the RCP scenarios ranges from 1.0 to 4.5°C relative to 1850–1860 mean temperature in the historical simulations. In the RCP2.6 scenario, the surface warming in all simulations stays below a 2°C threshold at the end of the 21st century. For RCP8.5, the range is 3.5–4.5°C at 2100. Decadally averaged sea ice area changes are highly correlated to global mean surface air temperature anomalies and show steep declines in both hemispheres, with a larger sensitivity during winter months. By the year 2500, there are complete recoveries of the globally averaged surface air temperature for all versions of the GISS climate model in the low-forcing scenario RCP2.6. TCADI simulations show enhanced warming due to greater sensitivity to CO_2, aerosol effects, and greater methane feedbacks, and recovery is much slower in RCP2.6 than with the NINT and TCAD versions. All coupled models have decreases in the Atlantic overturning stream function by 2100. In RCP2.6, there is a complete recovery of the Atlantic overturning stream function by the year 2500 while with scenario RCP8.5, the E2-R climate model produces a complete shutdown of deep water formation in the North Atlantic.

1. Introduction

There is a long-standing concern that increases in the concentrations of greenhouse gases and aerosols from human activity will lead to substantial changes in Earth's climate in the 21st century. There is already evidence that anthropogenic emissions of greenhouse gases have altered the large-scale patterns of temperature and other variables over the twentieth century [*Meehl et al.*, 2007; *Hegerl et al.*, 2007]. The future anthropogenic climate responses have large uncertainty due to uncertainty in the climate sensitivity to the increasing greenhouse gases (a consequence of physical and modeling uncertainties) and the challenge of anticipating future atmospheric composition and forcing [*Hawkins and Sutton*, 2009]. Two key uncertainties lie in the behavior and impact of short-lived species, such as tropospheric aerosols and ozone, and, second, in the response and impact of the ocean circulation.

Climate models including representations of relevant physical, dynamical, and chemical processes are essential tools for estimating the responses to ongoing and future drivers, as well as for exploring potential feedbacks and sensitivities. The Coupled Model Intercomparison Project phase 5 (CMIP5) [*Taylor et al.*, 2012] includes simulations of 21st century climate with four different Representative Concentration Pathway (RCP) scenarios and extensions of the climate change projections from 2100 to 2300 [*van Vuuren et al.*, 2011a]. Given physically consistent emission scenarios of land use, greenhouse gases, aerosols, and other anthropogenic precursor gases, understanding the climate response to the resulting anthropogenic forcings and the interactions between climate change, atmospheric chemistry feedbacks, and transport processes is still a major challenge.

Here we use the GISS-E2 climate model [*Schmidt et al.*, 2014a] to explore the sensitivity of the model response to varying treatments of atmospheric composition and two different ocean models. The wide range of the 21st century RCP scenarios allows us to see the impact of different magnitudes of anthropogenic forcings, as well as the response of the climate system simulated with different model representations. The credibility of the future simulations depends on how the climate model reproduces the preindustrial, historical, and current conditions, processes, and sensitivities. Many comparisons to observations are described in *Schmidt et al.* [2014a]. Using observed historical anthropogenic and natural forcings, the twentieth century warming trends in temperature, sea ice, ocean heat content, etc. are within the uncertainty of the observed values [*Miller et al.*, 2014; *Shindell et al.*, 2013a].

The main focus of this paper is to provide an overview and description of the GISS climate simulations of the 21st century RCP scenarios and their extensions, to provide estimates of global climate change and impacts on regional scales with different versions of the GISS climate model. The paper by *Schmidt et al.* [2014a] describes the GISS climate model including improvements of model physics as well as the comparison of the modern climatology of the atmospheric and coupled models to the latest available observational data from satellite and ground measurements. Another companion paper by *Miller et al.* [2014] discusses the simulations of climate change over the CMIP5 "historical period" 1850–2005. Many details of the interactive aerosol and chemistry are presented in two papers by *Shindell et al.* [2013a, 2013b].

In section 2, we present a brief description of different versions of the GISS climate model, as well as the model sensitivities and transient climate responses. Section 3 describes the Representative Concentration Pathways (RCP) scenarios and forcings applied for 21st century simulations. The results of the RCP scenario experiments for the global changes are discussed in section 4, for the regional changes—in section 5, for the extensions from 2100 to 2500—in section 6, and for normalized response—in section 7. Conclusions will be presented in section 8.

2. Model Description

2.1. Atmospheric Models

We use the new version of NASA Goddard Institute for Space Studies (GISS) climate model, ModelE2 (denoted GISS-E2 in the CMIP5 archive) with $2° \times 2.5°$ horizontal resolution and 40 vertical layers, with the model top near the stratopause at 0.1 hPa. The basic physics of the model is similar to the CMIP3 version of GISS ModelE [Schmidt et al., 2006] but includes numerous improvements to the physics as reported in *Schmidt et al.* [2014a, 2014b]. We use three different treatments of the atmospheric composition. The simplest is a version with NonINTeractive (NINT) composition, i.e., using prescribed three-dimensional distributions of ozone and aerosols interpolated from the decadal concentrations. These decadal distributions of ozone and aerosols for the historical 1850–2005 simulations are obtained from the off-line calculations of a previous version of the stand-alone atmospheric model with interactive chemistry [*Koch et al.*, 2011]. The aerosol indirect effect on clouds is included as a simple parameterization for increasing the low-cloud cover in response to increasing aerosols [*Hansen et al.*, 2005a]. This parameterization is based on an assumed relation between aerosol number concentrations and clouds and tuned to produce a roughly -0.7 W m^2 TOA radiative imbalance in 2000 relative to 1850 (see *Miller et al.* [2014] for a discussion).

The second version (TCAD) has fully interactive Tracers of Aerosols and Chemistry (including Direct effects; TCAD) in both the troposphere and stratosphere. All chemical species are simulated prognostically consistent with atmospheric physics in the model and the emissions of short-lived precursors [*Shindell et al.*, 2006]. The indirect effect of aerosols is parameterized in the same way as in the NINT version. The third version

additionally includes a parameterization of the first indirect aerosol effect on clouds (TCADI) following *Menon et al.* [2010]. Increased aerosol concentration leads to the decrease of cloud droplet size, which makes clouds brighter and more reflective [*Twomey*, 1977]. In the CMIP5 archive, the NINT, TCAD, and TCADI runs are noted using physics-version 1, 2, and 3, respectively.

2.2. Ocean Models

We couple two different ocean general circulation models to each of the three atmospheric versions. In neither case do we use any flux corrections in the heat exchange between atmosphere and ocean. The "Russell ocean model" was originally described by *Russell et al.* [1995]. This ocean model is a mass-conserving with horizontal resolution of 1.25° longitude by 1° latitude, and has 32 vertical levels with finer resolution in the top 100 m. The model uses the C-grid for the momentum equations, which includes the KPP parameterization for vertical mixing [*Large et al.*, 1994] and the Gent-McWilliams parameterization for the mixing effect associated with mesoscale eddies [*Gent and McWilliams*, 1990]. In the CMIP5 archive, the climate model with the Russell ocean model is referred to as GISS E2-R (henceforth E2-R in this text).

The other ocean model used for climate simulations is HYCOM [*Bleck*, 2006; *Sun and Bleck*, 2006], the HYbrid coordinate version of the Miami Isopycnal Coordinate Ocean Model. The model maintains an isopycnal coordinate representation in the oceanic interior but allows coordinate layers to become constant in depth poleward of the location where their "target" isopycnals outcrop. The presence of a fixed number of vertical layers (26 in this case) allows vertical mixing in HYCOM to be simulated as a cross-isopycnal diffusion process. The horizontal resolution is 1° both in latitude and longitude, with meridional resolution gradually increasing to 1/3° equatorward of ±30° latitude. Vertical mixing is based on a Kraus-Turner-type turbulent kinetic energy closure. In the CMIP5 archive, the climate simulations with the HYCOM ocean model are referred to using GISS E2-H (henceforth E2-H).

Both ocean models include the same model of sea ice in the Arctic and Antarctic [*Zhang and Rothrock*, 2000; *Russell et al.*, 2000].

2.3. Model Biases, Drifts, and Sensitivity

The GISS-E2 simulations have some biases for the current climate. Although the sea ice climatology and seasonality are improved in all current versions of the GISS-E2 climate model compared to the CMIP3 results [*Hansen et al.*, 2007], the models overestimate the seasonal cycle of the Arctic sea ice with a too low September minimum [*Schmidt et al.*, 2014a]. This leads to smaller than observed initial sea ice conditions in the Arctic for all RCP experiments, and this is especially obvious for all versions of the GISS E2-H due to their much warmer surface temperatures in the high northern latitudes. The RCP experiments with the GISS E2-H consequently started with too small September sea ice cover in the Arctic Ocean which leads to rapid sea ice melting and a summer ice-free Arctic around 2040–2050 in all those RCP experiments (see section 4.2 for more details). In the Southern oceans, all GISS models are too warm and have deficient Antarctic sea ice.

The control experiments for 1850 atmospheric composition have drift of 0.001, 0.05, and 0.02°C per century for the NINT, TCAD, and TCADI E2-R climate models, respectively, and 0.01, 0.05, and 0.05°C per century for the NINT, TCAD, and TCADI E2-H coupled models, respectively. Anomalies for each perturbation experiment are calculated by removing a smoothed loess fit constructed from the control [*Miller et al.*, 2014, Figure 1] to account for nonclimatic drift due to the small disequilibrium in the initial conditions. However, we note that this drift is small compared to the 21st century climate trends discussed in this article. The global mean surface air temperatures are 14.3, 14.5, and 14.7°C at modeled year 1000 of the NINT, TCAD, and TCADI E2-R control climate models, respectively, 15, 15.2, and 15.2°C in the NINT, TCAD, and TCADI E2-H control climate models.

The coupled model equilibrium climate sensitivities for doubled CO_2 are 2.7, 2.7, and 2.9°C for the three atmospheric models NINT, TCAD, and TCADI [*Schmidt et al.*, 2014a], which is on the lower end of climate sensitivity of the CMIP5 models between 2.1 and 4.7 K [*Andrews et al.*, 2012]. The transient climate response (TCR) is the 20 year mean surface air temperature resulting from a 1% per year increase of CO_2, centered on the time of doubling, and relative to the corresponding 20 year mean temperature of the control simulation. The TCR depends upon the equilibrium climate sensitivity, but also the rate of heat uptake by the deep ocean. The transient climate responses are 1.4, 1.4, and 1.6°C for the NINT, TCAD, and TCADI E2-R climate models, respectively, and 1.7, 1.7, and 1.8°C for the NINT, TCAD, and TCADI E2-H coupled models.

These values are within the range of 1.1–2.3°C obtained from the constrained estimates of transient climate response based on observed global temperature and ocean heat uptake [*Lewis and Curry*, 2014; *Otto et al.*, 2013; *Knutti and Tomassini*, 2008; *Stott and Forest*, 2007].

3. Representative Concentration Pathways (RCP) Experiments

Because it is impossible to predict exactly the future emissions and other factors that affect climate, the development of a range of future scenarios with a wide range of various assumptions about future economic, social, technological, and environmental conditions allows us to assess a wide range of contingencies on global and regional scales. A set of four new future scenarios, the so-called Representative Concentration Pathways (RCPs), was developed as a basis for the CMIP5 long-term and short-term modeling experiments [*van Vuuren et al.*, 2011a]. These future scenario simulations are continuations of the historical experiments, 1850–2005, and begin on 1 January 2006.

The four RCPs reflect the range of year 2100 greenhouse gas radiative forcing values from 2.6 to 8.5 W m^{-2} (Figure 1): the lowest forcing level scenario RCP2.6 [*van Vuuren et al.*, 2011b], two median range or stabilization scenarios RCP4.5 [*Thomson et al.*, 2011] and RCP6.0 [*Masui et al.*, 2011], and the high-end or business-as-usual scenario RCP8.5 [*Riahi et al.*, 2011]. The net forcing is determined by both positive forcing from greenhouse gases and negative forcing from aerosols, though the dominant factor across the scenarios is the forcing from CO_2 (Figure 2). Radiative forcings from the land use scenarios are relatively small compared to radiative forcings from greenhouse gases, although deforestation is an important element in the CO_2 emissions. Note that the actual radiative forcing values at 2100 for different RCP scenarios will depend on the climate model and on included feedbacks that affect atmospheric composition (for instance, related to CH_4 or carbon feedbacks). Figure 1 shows that the radiative forcings for all RCP scenarios are larger than the nominal forcing in the GISS-E2 model. This is mainly due to a different radiative forcing associated with doubled CO_2, which is 4.2 W m^{-2} in our model versus the canonical 3.7 W m^{-2} [*Ramaswamy et al.*, 2001]. If a scaling is applied based on this difference, the RCP scenario radiative forcings are close to the assessed values in the scenarios.

The land use projections are very wide-varying in different RCPs. In RCP8.5, there are increases in croplands and grasslands due to increasing global population. In RCP2.6, there is also increase in croplands as a result of bio-energy production. The decrease in the grasslands is applied in three RCP scenarios, except RCP8.5, based on the implementations of shifts from extensive to more intensive animal farming. The RCP6.0 shows an increasing use of cropland but a decline in pasture. This decline is caused by a similar trend as noted for RCP2.6, but with a much stronger implementation. Finally, the RCP4.5 shows a clear turning point in global land use based on the assumption that carbon in natural vegetation will be valued as part of global climate policy. As a result of reforestation programs, the use of cropland and grassland decreases, following considerable yield increases and dietary changes [*van Vuuren et al.*, 2011a].

In all RCP scenarios and models, volcanic aerosols are repeated from the year 2000. For the solar forcing, we repeat the last 11 year solar cycle that ended in 2008. N_2O and CFC concentrations (Figure 2) are provided by RCP projections [van Vuuren et al., 2011a]. For both of these drivers the post-2000 evolution in the real world has been significantly different to what was assumed. In the historical simulations from 2005 to 2012,
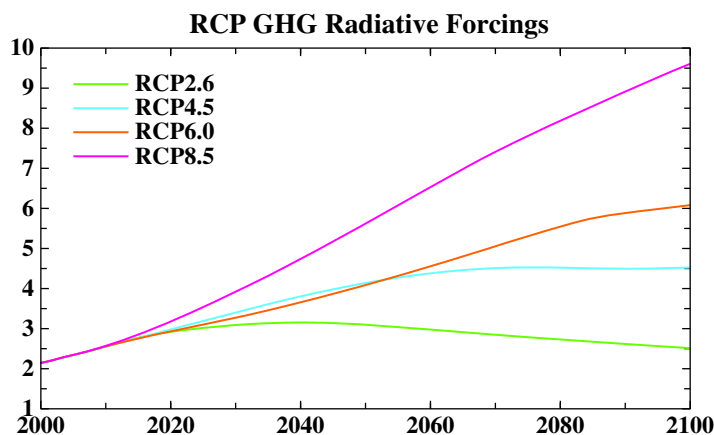
Figure 1. Instantaneous global GHG climate forcings diagnosed for global future climate simulations relative to their values in 1950 in the GISS-E2 models. Green line: RCP2.6 [*van Vuuren et al.*, 2011b], light blue line: RCP4.5 [*Thomson et al.*, 2011], orange line: RCP6.0 [*Masui et al.*, 2011], and pink line: RCP8.5 [*Riahi et al.*, 2011].
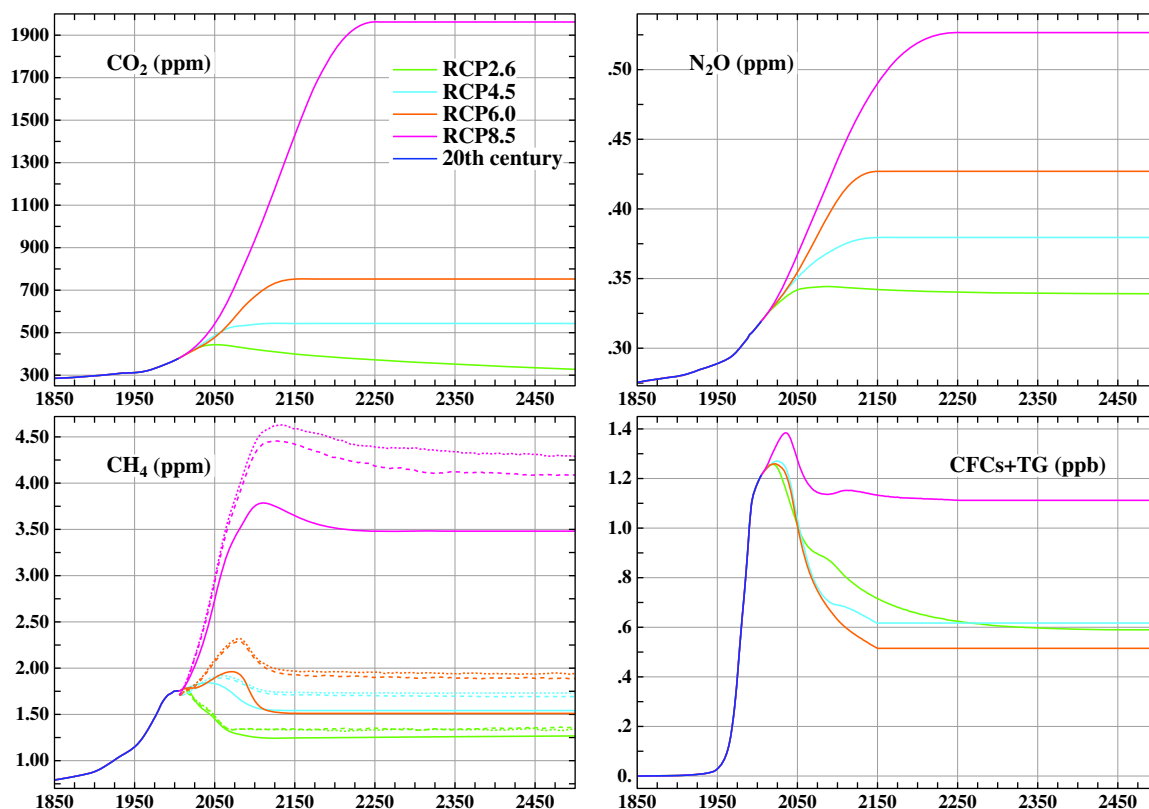
Figure 2. Greenhouse gas mixing ratios in the RCP scenarios (colors and references as for Figure 1 with additional blue line showing observations [Hansen and Sato, 2004]. The dotted/dashed lines for the resultant CH_4 are from the TCAD and TCADI experiments which include methane wetland and chemistry feedbacks.

concentrations of CO_2, N_2O, and CH_4 were lower than used in the RCP scenarios, whereas CFCs were a little higher [*Schmidt et al.*, 2014b]. More details about the extension of historical runs from 2005 to 2012 are presented in *Miller et al.* [2014].

In the NINT RCP experiments, the active radiative forcing components are limited to the greenhouse gases and land use projections. Both tropospheric aerosols and ozone are kept constant at the 1991–2000 mean. The aerosol emissions used in the NINT models are based on the emission database for global atmospheric research and global fire emissions database [*Van Aardenne et al.*, 2001; *Bond et al.*, 2004]. For stratospheric ozone, there is a recovery of ozone concentrations by 2050.

In the TCAD and TCADI models with interactive chemistry, CH_4 concentrations are calculated based on prescribed emissions and prognostic atmospheric chemistry. Both models show higher methane concentrations (Figure 2, the dotted and dashed lines) than the ones from the prescribed RCP concentrations (Figure 2, solid lines) [*Shindell et al.*, 2013a]. The RCP tropospheric ozone and aerosol concentrations are calculated in the TCAD and TCADI models in addition to the GHG and land use agents. The aerosol concentrations are driven by the RCP aerosol and precursor emissions based on inventory estimates for the RCP scenarios [*van Vuuren et al.*, 2011a] and include climate-related feedbacks on their sources, sinks, and transports.

In the scenario with the lowest radiative forcing RCP2.6, there is a substantial decline of CO_2 concentration from 421 ppm in 2100 to 328 ppm by 2500, as well as a decrease in concentration of the CFCs and other trace gases from 0.8 ppb from 2100 to 0.6 ppb to 2500. Nitrous oxide (N_2O) and methane (CH_4) are kept constant at year 2100 values.

The stabilization scenario RCP4.5 is characterized by very small increases of CO_2 and N_2O concentrations by 4.6 and 0.007 ppm from 2100 to 2150, respectively, and then the mixing ratios of these two greenhouse gases are kept constant. The concentrations of methane and CFCs and other trace gases decrease by 0.03 ppm and 0.07 ppb by the year 2150 and are not changing after that. The other medium-range scenario RCP6.0 has

larger increases in the concentrations of CO_2 and N_2O by 82 and 0.02 ppm between 2100 and 2150. It has some compensating decreases in other greenhouse gases, such as CH_4, CFCs, and other trace gases to maintain the radiative forcing at about 6 W m^2. The reductions are larger for other GHGs in the RCP6.0 scenario compared to RCP4.5 (0.14 ppm for CH_4 and 0.12 ppb for CFCs and other trace gases from 2100 to 2150).

The business-as-usual scenario RCP8.5 more than doubles the increase of the CO_2 concentration from 936 to 1962 ppm between 2100 and 2250. Small decreases in mixing ratios for CH_4, CFCs, and other trace gases do not play much of a role in the overall warming.

In the climate models with fully interactive composition, calculated CH_4 concentrations from emissions and prognostic chemical sinks are higher by about 0.08, 0.17, 0.4, and 0.71 ppm at the year 2500 for RCP2.6, RCP4.5, RCP6.0, and RCP8.5, respectively, than for the same RCP scenarios in the NINT configuration. As noted by *Shindell et al.* [2013b], the radiative forcing from methane is from 0.05 to 0.18 W m^2 higher in the TCAD and TCADI models than in the prescribed RCP methane radiative forcing estimates.

We carried out an ensemble of five runs for the RCP4.5 scenario using all versions of the GISS climate model, while for the three other RCP experiments, we conducted single runs for the 21st century and 400 years of their extensions (Figure 2). For the line plots of the annual mean quantities for each RCP scenario, the data were averaged for all versions of atmospheric and ocean models. The range of the RCP experiments is given by different shading for each RCP case. The maps present the means of two models with different oceans for RCP2.6, RCP 6.0, and RCP8.5, and the means of two five member ensembles of E2-R and E2-H for RCP4.5. To compare the regional difference between TCAD and NINT, TCADI, and NINT, and E2-H and E2-R, the averages were made over all versions of E2-R and E2-H simulations for RCP4.5.

4. Global Changes

4.1. Global Temperature and the Planetary Energy Imbalance

Figure 3 shows the simulated global mean surface air temperature (drift-corrected) anomalies relative to the 1850–1880 base period. During the historical simulation from 1850 to 2005, the global mean surface air temperature essentially follows the estimated global mean forcing through time, showing cooling following the short-term forcing by volcanic aerosols and strong warming for a few decades at the end of the twentieth century due to the dominant positive forcing of the increasing greenhouse gases. Simulated global warming ranges from 0.9 to 1.3°C between 1880 and 2005 and agrees well with the observed temperature increase, which is estimated as 0.9°C (see *Miller et al.* [2014] for more discussion of the twentieth century changes and comparison to observations).

The RCP experiments begin in 2006. Relative to the 1996–2005 mean temperature in the historical simulations, simulated global warming ranges from 0.4 to 2.0°C at 2050 (Table 1). For both intermediate RCP4.5 and RCP6.0 (Figure 3) scenarios, the warming of the global mean surface air temperature increases and exceeds 1°C by 2100. In the RCP2.6 scenario, the warming decreases from a 0.4–1.1°C, peak at 2050, to 0.2–1.0°C by 2100 reflecting the peak of radiative forcing at the midcentury and subsequent decline (Figure 1, green line). In contrast, the warming in RCP8.5 (Figure 1, solid pink line) approaches 3.7°C by 2100. The TCADI model generally shows larger warming than the other two models TCAD and NINT (Table 1) that is partly a consequence of the higher TCADI model climate sensitivity. Some explanations of stronger warming in the TCADI coupled model are given in the section 4.4 for the regional changes. The E2-H models
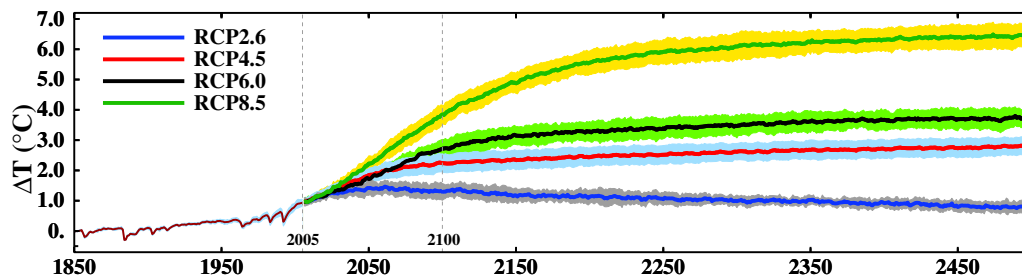
Figure 3. Global annual mean surface air temperature anomalies relative to 1850–1880 base period for all RCP scenarios. Different shadings indicate ranges of the RCP experiments with the NINT, TCAD, and TCADI E2-R and E2-H climate models.

Table 1. Surface Air Temperature Change (°C) Relative to (1996–2005) Mean Temperature for Different Years in the Future

RCP Scenarios	2050	2100	2200	2300	2400	2500	2100[a]
RCP2.6 NINT-ER	0.5	0.2	0.2	0.1	0.0	−0.1	1.0
NINT-EH	0.7	0.5	0.4	0.2	0.0	−0.1	1.5
TCAD-ER	0.4	0.3	0.2	0.1	0.0	−0.1	1.0
TCAD-EH	1.0	0.7	0.3	0.0	0.0	−0.2	1.5
TCADI-ER	0.8	0.8	0.7	0.6	0.4	0.4	1.8
TCADI-EH	1.1	1.0	0.8	0.5	0.4	0.2	1.8
RCP4.5 NINT-ER	0.9	1.1	1.3	1.5	1.5	1.7	1.9
NINT-EH	1.1	1.4	1.5	1.6	1.8	1.8	2.4
TCAD-ER	0.9	1.3	1.4	1.6	1.7	1.8	2.0
TCAD-EH	1.3	1.6	1.7	1.8	2.0	2.1	2.3
TCADI-ER	1.1	1.7	2.0	2.1	2.2	2.4	2.6
TCADI-EH	1.4	1.9	2.1	2.1	2.3		2.9
RCP6.0 NINT-ER	0.8	1.6	2.1	2.2	2.6	2.6	2.4
NINT-EH	1.1	2.0	2.5	2.7	2.8	2.9	2.9
TCAD-ER	0.8	1.6	2.3	2.3	2.5	2.7	2.4
TCAD-EH	1.3	2.1	2.7	2.8	3.0	3.1	2.9
TCADI-ER	0.8	2.3	2.9	3.1	3.3	3.2	3.2
TCADI-EH	1.4	2.5	3.0	3.3	3.4	3.5	3.4
RCP8.5 NINT-ER	1.3	2.7	4.2	4.8	5.0	5.3	3.5
NINT-EH	1.6	3.1	4.8	5.3	5.5	5.6	4.1
TCAD-ER	1.2	2.8	4.6	4.8	5.2	5.5	3.5
TCAD-EH	1.7	3.3	4.9	5.4	5.6	5.8	4.1
TCADI-ER	1.6	3.4	5.1	5.9	6.0	6.1	4.3
TCADI-EH	2.0	3.7	5.5	5.9	6.1	6.4	4.5

[a]The 2100 column is surface air temperature change (°C) relative to (1850–1860) mean temperature.

produce warmer surface air temperatures in most cases than their E2-R counterparts due to a reduced ocean heat uptake in E2-H model (which has a stronger Transient Climate Response (TCR)).

A global threshold of "dangerous" climate change has been proposed at 2°C above the preindustrial surface air temperature [*Meinshausen et al.*, 2009]. The last column in Table 1 shows the year 2100 surface air temperature change relative to (1850–1860) mean temperature of the relevant historical simulation. Only the simulation under RCP2.6 has surface warming below 2°C by the end of the 21st century. This is achieved as a consequence of the CO_2 emissions decreasing at the middle of the 21st century and becoming net negative by 2100. Two model versions, NINT E2-R and TCAD-E2-R, simulate 21st century warming close to the threshold proposed by Meinshausen et al. [2009] in the RCP4.5 scenario, while the other versions of GISS climate model exceed the threshold in the RCP4.5 scenario. All model versions for RCP6.0 and RCP8.5 scenarios exhibit substantially greater than 2°C warming at 2100, with the range of the surface temperature increases between 2.4 and 4.5°C.

The planetary energy imbalance (Figure 4) reflects the impact of the global GHG and non-GHG forcings applied in different RCP scenarios (Figure 1) combined with the radiative feedbacks which respond to the change in temperature (Figure 3). It is also a good proxy for the rate of accumulation of heat in the ocean and thus for the thermal component of sea level rise [Hansen et al., 2005b]. There is a definite decline of the energy imbalance to half of its maximum value in RCP2.6 by the year 2100, implying the eventual achievement of a future equilibrium state after a few additional centuries of simulation. In RCP4.5, a small decrease of energy imbalance is also seen reflecting the stabilization of GHG forcing in the last 30–40 years of the 21st century (Figure 1). In RCP6.0 and RCP8.5 with stronger and continually increasing radiative forcing, there is a continuous increase of the energy imbalance to 2100. Afterward, there is a gradual imbalance decrease in the scenario RCP6.0 following strong decreases of CH_4, CFCs, and other trace gases. No change of the imbalance is observed between 2100 and 2250 in the case RCP8.5 that reflects a large increase of the CO_2 concentration.

4.2. Sea Ice Changes

After temperature, a visible sign of climate change is the state of the sea ice, particularly in the Arctic. Rapid decreases over the last few decades (most noticeable in September) have led to speculation concerning the unexpectedly quick disappearance of summer sea ice. Projections of sea ice decline, however, are quite sensitive to errors in the base climatology [*Massonnet et al.*, 2012] and so raw model projections may not be very reliable. While annual means and trends in the historical period for the Arctic are well simulated in the
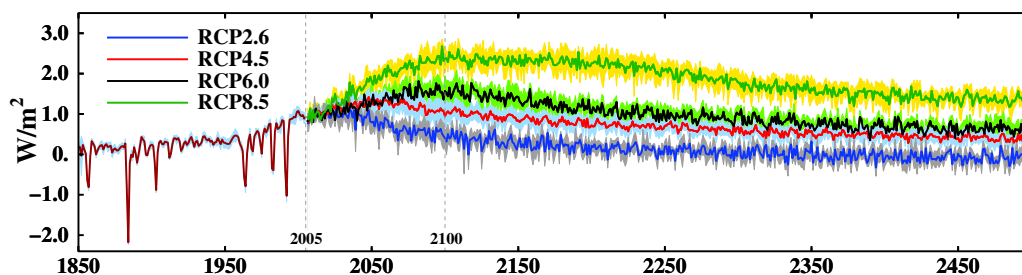
Figure 4. Net radiation at the top of the atmosphere (W m^2).

E2-R models [*Miller et al.*, 2014], there are offsets in seasonality and too little ice in the E2-H runs [*Schmidt et al.*, 2014a]. Simulations of the southern hemisphere sea ice are not as realistic, particularly in the summer.

The E2-R models have larger sea ice cover initially compared to the sea ice cover in the corresponding E2-H runs. However, both models have a seasonal cycle with excessive amplitude compared to observations [*Schmidt et al.*, 2014a]. In response to stronger warming, the TCADI model produces more sea ice melt than the other atmospheric variants using both ocean configurations and in all RCP experiments. For RCP8.5, the E2-H model shows the largest decrease (48 and 55% for the annual mean sea ice cover based on linear trends) over the period 2006–2100 for the Northern and Southern Hemispheres, respectively, averaged over all three (NINT, TCAD, and TCADI) configurations. The sea ice decreases in other RCP scenarios are smaller and proportional to respective forcings.

E2-R shows a recovery of Northern Hemisphere annual mean sea ice cover in the second half of the 21st century in the RCP2.6 experiments with the NINT and TCAD configurations (by 3.7 and 3%, respectively). However, the TCADI model produces more sea ice melt (7.6% decrease), reflecting the stronger warming in this model compared to the other two. In the Southern Hemisphere, the annual mean sea ice in the RCP2.6 decreases by 11.2% averaged over three models with different atmospheric configurations. All other RCP experiments with E2-R models show substantial decreases of the annual averaged sea ice cover (Table 2).

In all RCP scenarios, both E2-R and E2-H produce relatively faster declines of the Northern Hemisphere sea ice cover in September (Figure 5e) except for the two RCP2.6 experiments with the NINT and TCAD E2-R models (two red dots in the upper left corner in Figure 5e). The Arctic reaches ice-free summer conditions (defined as less than 1.0×10^6 km^2 following *Stroeve et al.* [2012a]) around 2040 in TCADI E2-R RCP2.6 and in all E2-R RCP4.5, and around 2025 in RCP6.0 in E2-R model while the RCP8.5 experiments show essentially ice-free conditions in September from the start of the 21st century which results from the strong warming. In both E2-R and E2-H models, the uncertainty of September ice-free Arctic is 10–15 years due to different initial conditions for each ensemble member in the RCP4.5.

The E2-H model starts off with less sea ice at 1850. After the Northern Hemisphere sea ice melt during the twentieth century, the September sea ice area is unrealistically smaller than 1.0×10^6 km^2 at the beginning of all RCP experiments. The extensive decrease of Arctic summer sea ice cover is due to simulated bias in the seasonal cycle of the Northern Hemisphere sea ice with too little sea ice area in September and too much ice in March [*Schmidt et al.*, 2014a] in the control simulation with the preindustrial atmospheric composition at the year 1850, which leads to substantially less sea ice by the end of the historical simulation at the year 2005. The minimum observed September Northern Hemisphere sea ice area was reported as about 3.0×10^6 km^2 in 2007 [*Stroeve et al.*, 2012b]. Both the E2-R and E2-H coupled models underestimate the Arctic sea ice cover even for the exceptional year of 2007.

The Southern Hemisphere has very little ice in March at the beginning of all RCP experiment (Figure 5d). Both the E2-R and E2-H models underestimate the Southern Hemisphere sea ice area in the historical simulations of the twentieth century climate [*Miller et al.*, 2014]. Except for the Southern Hemisphere in the RCP2.6, stronger warming in the coupled model E2-H produces more sea ice melting relative to E2-R.

Notwithstanding the biases in the climatology, it is instructive to examine the variability and relationships between the global annual mean (2040–2059) surface air temperature and the Northern and Southern sea ice areas (10^6 km^2) for annual, March, and September (2040–2059) (Figure 5). The sensitivities of the sea ice to the global warming (defined as the slopes of the regression lines) are largest for annual mean Northern

Table 2. Annual Mean Sea Ice Cover Decrease Based on Linear Trend Over the Period 2006–2100

	RCP2.6	RCP4.5	RCP6.0	RCP8.5
	NH SH	NH SH	NH SH	NH SH
E2-H	8% 10%	26% 34%	32% 32%	48% 55%
E2-R	0.33% 11%	16% 12%	19% 16%	33% 22%

Hemisphere sea ice cover in both E2-R and E2-H models (Figure 5a). The regressions -1.24×10^6 km^2/°C for E2-R and -1.44×10^6 km^2/°C for E2-H are comparable to the sensitivity of the Arctic (70°N–90°N) sea ice area to global warming in CMIP models surveyed by *Roeckner et al.* [2012], which ranges between -1.3×10^6 and -1.7×10^6 km^2/°C for the annual mean sea ice cover in four different realizations of RCP4.5. The summer sea ice cover is more sensitive to global warming in E2-R models than in E2-H models in both hemispheres (Figures 5e and 5d) reflecting the situation of smaller sea ice cover in E2-H models. The stronger summer sensitivity of sea ice to the temperature increase is supported by the observed extreme shrinkage of the Arctic ice in September over the last years [*Stroeve et al.*, 2012b]. The cold season sea ice cover is much less sensitive to the change in annual mean surface air temperature (Figures 5c and 5f) in both models.

4.3. Ocean Heat Content and Thermosteric Sea Level Changes

Due to the impact of large-scale warming on North Atlantic Ocean density, there is a decrease in the overturning stream function of 36–65% in the RCP8.5 experiments relative to the corresponding control simulations by the end of the 21st century. In RCP4.5 and RCP6.0, there are 35–45% reductions of the Atlantic
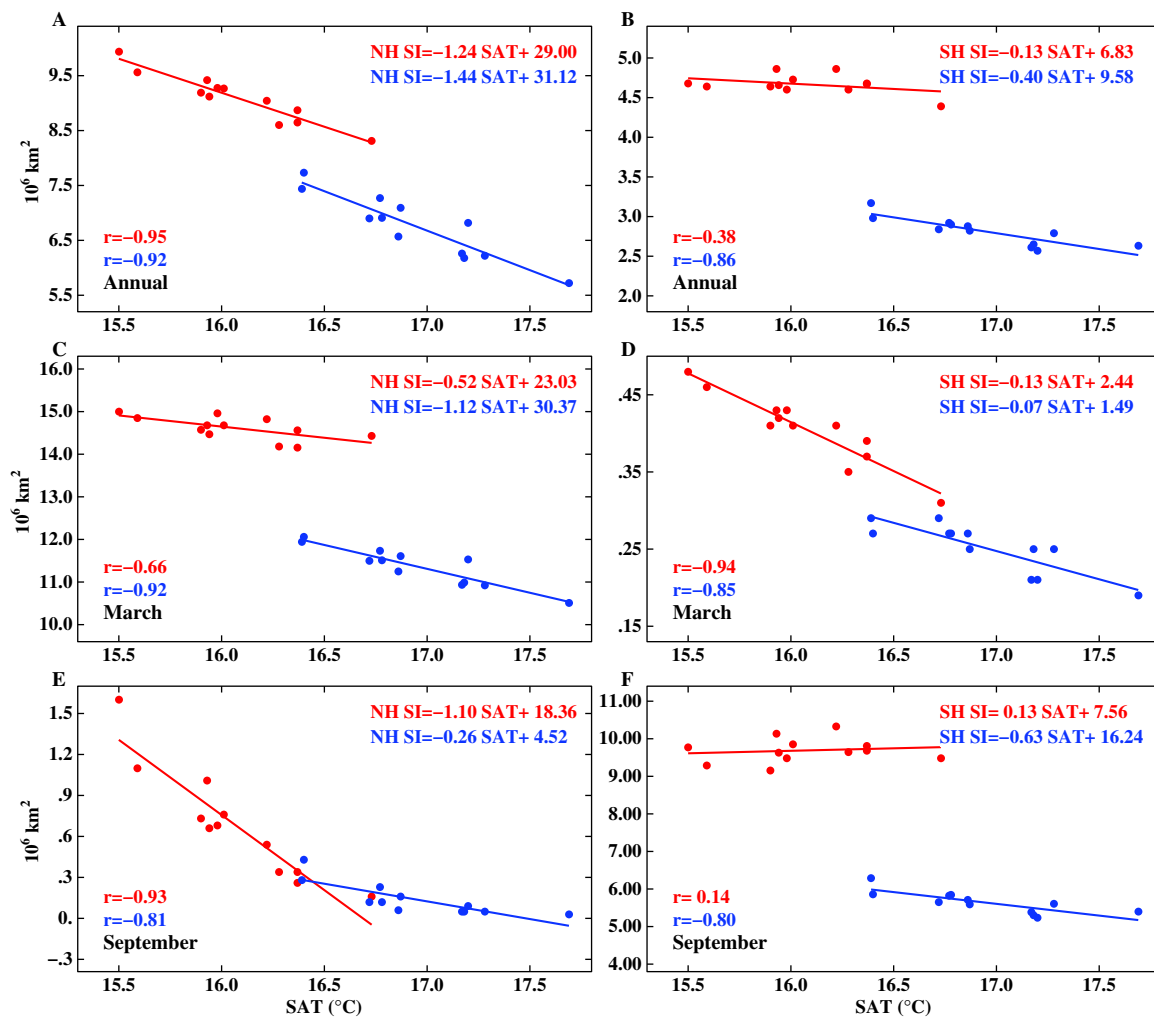
Figure 5. Relationship between the global annual mean (2040–2059) surface air temperature and sea ice area (10^6 km^2). (a) Annual (2040–2059) mean Northern Hemisphere sea ice area; (b) annual (2040–2059) mean Southern Hemisphere sea ice area; (c) March (2040–2059) mean Northern Hemisphere sea ice area; (d) March (2040–2059) mean Southern Hemisphere sea ice area; (e) September (2040–2059) mean Northern Hemisphere sea ice area; (f) September (2040–2059) mean Southern Hemisphere sea ice area. Red dots are for E2-R models, blue dots are for E2-H models.

overturning in E2-R models and more moderate 20–25% slowing in E2-H climate models. In RCP2.6, there is only a slight weakening of the North Atlantic overturning is 1–3 Sv by 2100, which is within the range of the ocean internal variability. Interestingly, the response of the overturning is not a linear function of global mean temperature, but is rather a delayed response to the overall path of warming. This is discussed further below.

Insight into the ocean response can be gained by examining the changes of ocean heat content. Overall, the ocean is warmer in E2-R, and ocean warming in response to positive forcings is greater in E2-R compared to E2-H. The largest increases in ocean heat content from 2006 to 2100 are seen in the RCP8.5, with increases of 287.3×10^{22} J (10% relative to the year 2006 ocean heat content) in E2-R and 234.3×10^{22} J (9%) in E2-H. RCP4.5 and RCP6.0 show relatively similar ocean warming. RCP2.6 produces the weakest ocean warming of 134.3×10^{22} J (4.5%) in E2-R and 100.4×10^{22} J (3.8%) in E2-H. There is flattening in the increase of the ocean heat content in the RCP2.6 while more ocean warming persists in other RCPs due to the large thermal inertia of the ocean.

The ocean warming leads to an expansion of ocean volume. The observed trend of thermosteric sea level rise for the ocean above 700 m is 0.65 ± 0.12 mm per year [*Church et al.*, 2011] over the time period from 1993 to 2009. The results of the historical simulation for the same time period show thermal expansion of over 1 mm/yr including the deep ocean water masses [*Miller et al.*, 2014]. For all RCP scenarios with model E2-R, the simulated thermosteric sea level rise is shown in Table 3 (the results for coupled model E2-H are not included due to errors in the relevant diagnostics). The rate of thermosteric sea level rise is about the same in NINT and TCAD E2-R models for all RCP experiments, but is significantly greater in the TCADI model due to larger warming. Comparing the ocean level at the year 2100 to the preindustrial (1850–1860) mean sea level, the thermosteric sea level rises are 19–28, 27–34, 28–34, and 36–45 cm for RCP2.6, RCP4.5, RCP6.0, and RCP8.5, respectively. The difference between the highest RCP8.5 and lowest RCP2.6 scenarios is about 17 cm, which is comparable with 12.5 cm RCP scenario difference reported by Hallberg et al. [2013] for the two GFDL Earth System Models [*Dunne et al.*, 2012]. Note that sea level continues to rise through 2500 in the RCP2.6 scenario, despite recovery of temperatures to twentieth century values by this date. Although temperature begins to decrease by 2100, sea level increases by an additional 50% through the end of our simulations. This is a consequence of slow heat uptake by the deep ocean [*Meehl et al.*, 2005].

5. Regional Climate Changes

5.1. Surface Air Temperature
The geographical distributions of surface air temperature change for the last 20 years of the 21st century (2081–2100) relative to the 20 year base period (1986–2005) of the corresponding historical simulation are shown in Figure 6 for all four RCP scenarios. In this figure, the temperature changes are averaged over the NINT E2-R and E2-H climate models for each RCP scenario. The regional difference between TCAD and NINT, TCADI and NINT, and E2-H and E2-R are presented separately to demonstrate the distinctions between them (Figure 7). The number above the upper right corner is the global mean temperature change.

The geographical patterns of future surface temperature warming, such as polar amplification of temperature change and stronger warming over the continents, are similar to those obtained in previous model versions [*Hansen et al.*, 2007] and other models [*Meehl et al.*, 2007, 2012; *Giorgetta et al.*, 2013] and are similar in all four RCP scenarios (Figure 6). The warming over all continents in the RCP2.6 scenario (Figure 6a) is 4–5 times smaller than in the RCP8.5 case (Figure 6d) and 2–3 times smaller than in the RCP4.5 (Figure 6b) and RCP6.0 (Figure 6c) experiments. In all four RCP simulations, the warming is larger over land areas than over oceans, while greater over the Arctic and over the Northern Hemisphere high-latitude regions. There is the least warming over the northern area of the North Atlantic and over the large area of the Southern Ocean. The simulation with the smallest forcing RCP2.6 produces a small area of surface air temperature cooling of about $-0.5°C$ over a small area to the south of Greenland. This is a region of strong vertical convection in the North Atlantic where warm and salty water brought from tropics and subtropics cools from the cold Arctic air, becomes denser, and submerges to the lower ocean layers, the Northern section of the North Atlantic meridional overturning circulation.

Figure 7 demonstrates differences of five-run ensemble mean surface air temperature change for the late 21st century 2081–2100 minus 1986–2005 across the climate models for the RCP4.5 scenario. In this plot,

Table 3. Thermosteric Sea Level Rise (m) Relative to (1996–2005) Mean Sea Level for Different Years in the Future

RCP Scenarios	2050	2100	2150	2200	2250	2300	2100[a]
RCP2.6 NINT-ER	0.10	0.17	0.21	0.23	0.24	0.25	0.21
TCAD-ER	0.10	0.15	0.18	0.21	0.21	0.22	0.19
TCADI-ER	0.15	0.23	0.27	0.30	0.31	0.33	0.28
RCP4.5 NINT-ER	0.10	0.22	0.32	0.40	0.47	0.54	0.27
TCAD-ER	0.11	0.23	0.32	0.40	0.46	0.52	0.27
TCADI-ER	0.16	0.29	0.40	0.49	0.57	0.64	0.34
RCP6.0 NINT-ER	0.10	0.24	0.39	0.50	0.61	0.70	0.28
TCAD-ER	0.10	0.23	0.38	0.49	0.60	0.68	0.28
TCADI-ER	0.14	0.28	0.46	0.59	0.70	0.80	0.34
RCP8.5 NINT-ER	0.12	0.32	0.53	0.74	1.01	1.21	0.36
TCAD-ER	0.12	0.32	0.53	0.74	0.95	1.15	0.36
TCADI-ER	0.18	0.39	0.63	0.87	1.11	1.31	0.45

[a]The 2100 column is thermosteric sea level rise (m) relative to (1850–1860) mean sea level.

the temperatures are averaged over E2-R and E2-H simulations. Figure 7a shows that the TCADI atmospheric model with the highest climate sensitivity simulates stronger warming over almost all Earth areas except for a few areas of both northern and southern high latitudes. The temperature differences between NINT and TCAD are not statistically significant. The addition of the parameterized first aerosol effect on clouds makes the TCADI version significantly different to the TCAD configuration (Figure 7a). The decrease of the cloud cover in the TCADI models (Figure 14a) leads to large temperature increase relative to NINT and TCAD, except for a small area over the Southern Ocean. Figure 7c demonstrates the difference of surface air temperature change between climate models with different ocean components. E2-H produces much greater warming especially over the northern high latitudes, associated with less mixing of heat to the deep ocean and greater decrease of Arctic sea ice. Greater warming in the E2-H model is also seen for the global mean surface temperature time series for the RCP4.5 scenario (Table 1).

5.2. Precipitation

Figure 8 shows the geographical patterns of precipitation following Figure 6. Similar to the surface air temperature, the changes in precipitation are the smallest in the RCP2.6 (Figure 8a) and the largest in the RCP8.5 (Figure 8d). Precipitation increases along the Pacific intertropical convergence zone and along the equatorial ocean areas and decreases over much of the subtropics, which is the effect of more moisture
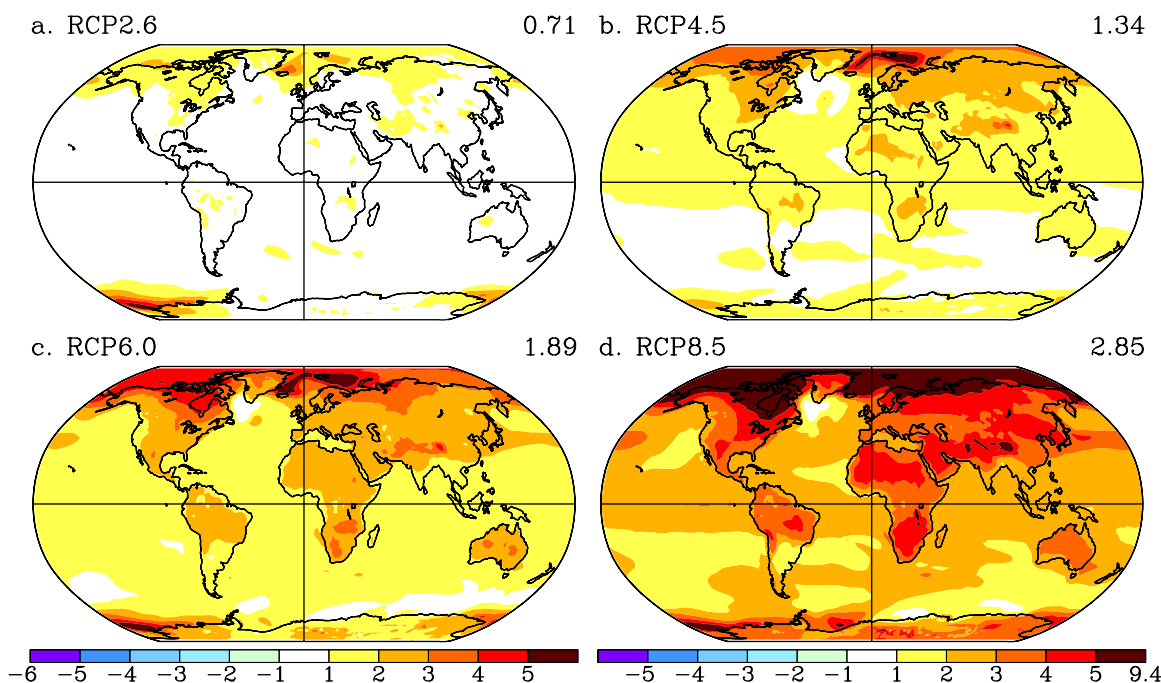
Figure 6. Surface air temperature differences (°C) for late 21st century 2081–2100 minus 1986–2005 of the corresponding historical ensemble member for the NINT climate model. (a) RCP2.6; (b) RCP4.5; (c) RCP6.0; and (d) RCP8.5.
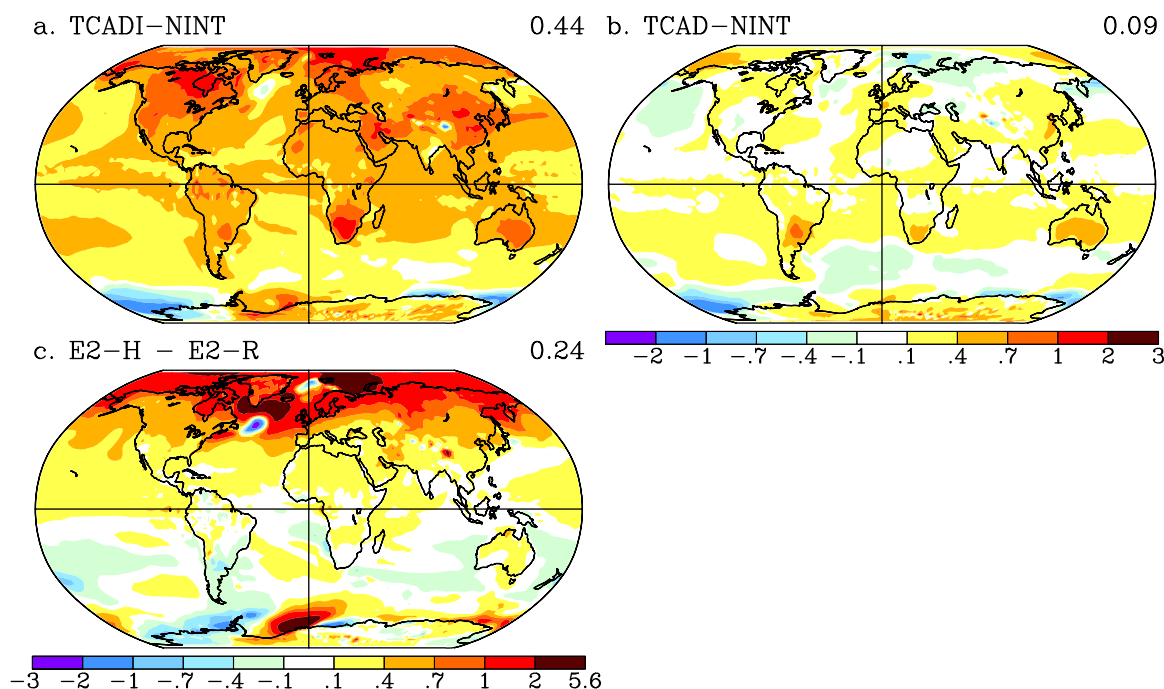
Figure 7. Differences of surface air temperature change (°C) in different climate models for the RCP4.5 scenario. (a) TCADI-NINT; (b) TCAD-NINT; and (c) E2-H minus E2-R.

convergence in the regions with already strong moisture convergence [*Held and Soden*, 2006; *Stevens et al.*, 2013]. There are increases in precipitation in the middle and high latitudes as the result of the enhanced poleward transport of moisture arising from the higher specific humidity in a warmer climate. Over land, precipitation increases over most of the Eurasian continent, North America, and southern areas of South America. The areas of precipitation decrease extend from the oceanic subtropics into the Amazon Basin, the Mediterranean, and the southern regions of Africa.

The climate models with interactive chemistry and aerosols TCADI and TCAD produce more rainfall change in equatorial ocean areas compared to the model with noninteractive aerosol chemistry (Figures 9a and 9b). Both the TCAD and TCADI models simulate enhancement of precipitation over the intertropical convergence zone, over the tropical and subtropical ocean areas. There is reduced precipitation over the equatorial Pacific in the E2-H model (Figure 9c) which is a reflection of stronger La Nina-like signal in this model. The Amazon Basin and the southern regions of Africa show increasing drying when the interactive aerosol chemistry is added to the atmospheric model. The areas over the Southern Ocean show reduced precipitation in all RCP experiments with the TCADI and TCAD models, relative to NINT, due to weaker warming over the these areas in the Southern Ocean (Figures 7a and 7b).

5.3. Sea Level Pressure

The simulated changes in the sea level pressure (Figure 10) show that the increasing greenhouse gas forcing tends to decrease the sea level pressure (SLP) over high northern and southern latitudes and increase the surface pressure in subpolar, midlatitude, and low-latitude bands. This is consistent with the notion that the greenhouse gas forcing produces an increasingly positive phase of the Arctic Oscillation [*Thompson and Wallace*, 1998, 2001; *Nazarenko et al.*, 2006, *Miller et al.*, 2006]. The increasing trend of the Arctic Oscillation was observed in the last few decades of the twentieth century, and a strong tendency for a winter trend has been reported in some climate models [*Shindell et al.*, 1999; *Dai et al.*, 2001; *Nazarenko et al.*, 2007]. In the study by *Miller et al.* [2014, Figure 24] shows the positive trend for leading principal component of the sea level pressure during the historical period and RCP8.5 scenario for all coupled model versions. The sea level pressure changes from different RCP scenarios (Figure 10) suggest that it is plausible to expect a trend toward the positive phase of the Arctic Oscillation with the increasing levels of the well-mixed greenhouse gases. An El Niño-like pattern with an SLP difference smaller over the eastern tropical Pacific than over the western tropical Pacific is also seen.
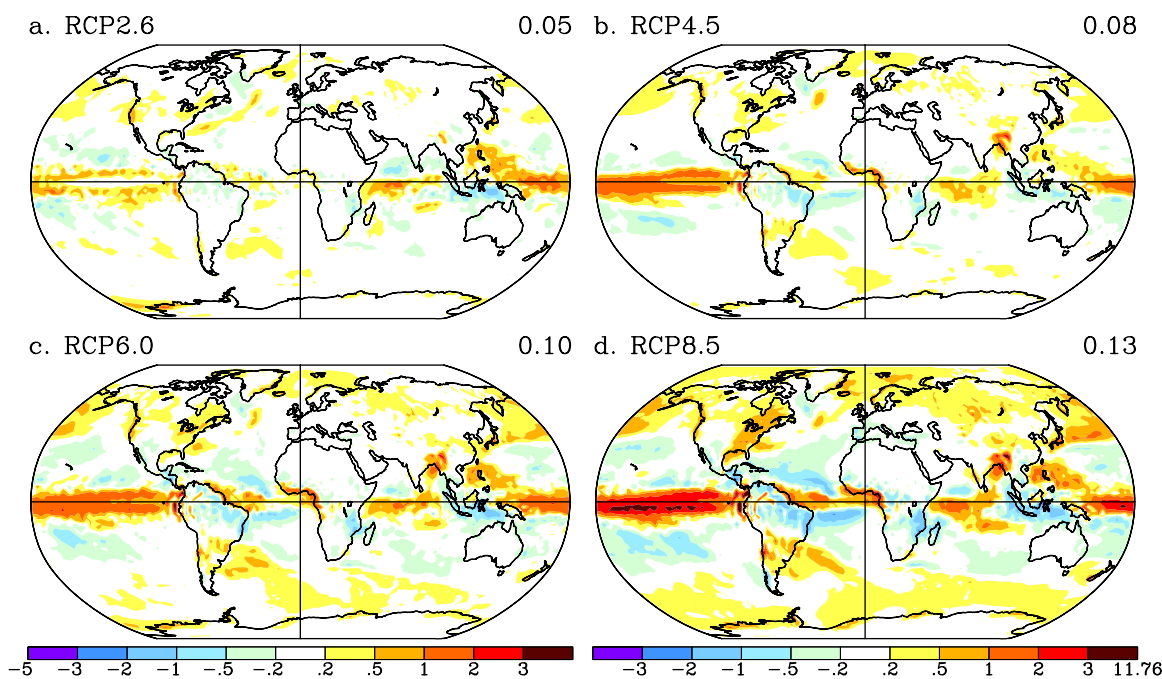
Figure 8. Precipitation differences (mm/d) for late 21st century 2081–2100 minus 1986–2005 of the corresponding historical ensemble member for the NINT climate model. (a) RCP2.6; (b) RCP4.5; (c) RCP6.0; and (d) RCP8.5.

From Figures 11a and 11b, it is evident that NINT models produce stronger SLP decreases over the Antarctica and greater SLP increases over the Southern Ocean than the interactive model versions, TCADI and TCAD. This is tied to the different realizations of the Antarctic ozone hole (prescribed in NINT, calculated in TCAD/TCADI). The positive-negative dipole-like SLP difference over the Southern Ocean characterizes the stronger Southern Oscillation variability in the E2-H coupled model (Figure 11c). The differences presented in Figure 11 are statistically significant at the 10% level.

5.4. Cloud Cover

Figure 12 presents the changes in the total cloud cover at the end of the 21st century. In previous model versions, global warming leads to a small overall decrease of cloud cover [*Yao and Del Genio et al.*, 1999; *Del Genio* et al., 2005]. In all four RCP scenarios, the current model has a reduction of both low and middle clouds and an increase in high clouds. This leads to enhanced short-wave warming due to reduced low-cloud reflection as well as to increased long-wave warming due to a stronger high-cloud greenhouse effect. The amplification of warming due to a reduction in low-level cloud cover occurs over tropical and subtropical ocean regions, and it was reported from an observational study combined with an analysis of model simulations [*Bony and Dufresne*, 2005; *Clement et al.*, 2009; *Brient and Bony*, 2013]. There are a few low-latitude regions of total cloud cover increase, especially over the eastern Pacific Ocean. There is an increase in high-level clouds at high latitudes.

Both TCADI and TCAD climate models predict more high and low-level clouds over the Southern Ocean reflected in total cloud cover changes (Figures 13a and 13b) which leads to reduced cloud short-wave and increased cloud long-wave radiative fluxes at the top of the atmosphere (Figures 14a and 14b). The net cloud radiative effect is small over the Southern Ocean resulting from canceling short-wave and long-wave radiative perturbations. Figure 14a shows the effect of different aerosol treatments on clouds. The low and total cloud cover decrease over some land areas, such as China and South America, is a little stronger in the TCADI models than in the NINT models (Figure 13a) resulting in increases of the short-wave (Figure 14a) and total cloud radiative forcing.

Figures 13a and 13d compare the effect of different treatments of the aerosol indirect effect on clouds in addition to different aerosol emissions. The simple parameterization for increasing low-level cloud cover response to increasing aerosols in the NINT and TCAD models produces more low and total clouds over
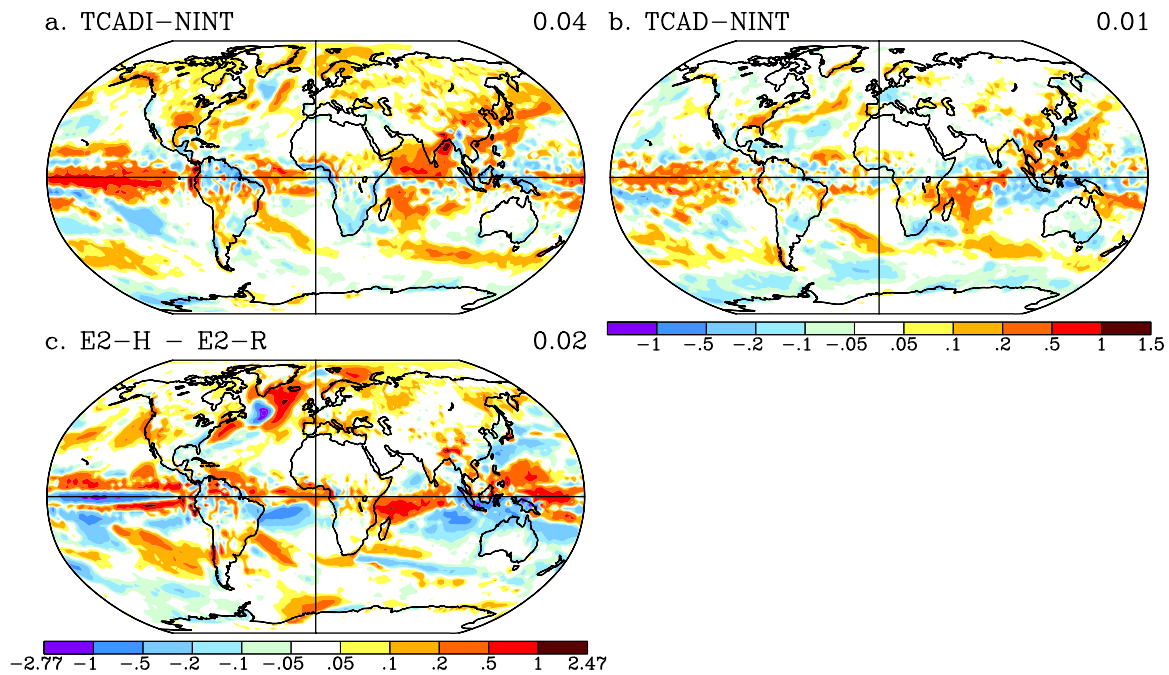
Figure 9. Differences of precipitation change (mm/d) in different climate models for the RCP4.5 scenario. (a) TCADI-NINT; (b) TCAD-NINT; and (c) E2-H minus E2-R.

most tropical and subtropical areas. This causes reduced short-wave cloud radiative forcing over most middle latitudes in the NINT (Figure 14a) and TCAD (Figure 14d) models. Different effects of time-varying tropospheric aerosol emissions in the TCAD models versus prescribed 1991–2000 mean aerosol concentrations in the NINT models is seen in reduced short-wave cloud radiative forcing over the Southern Ocean and over the high northern latitudes in the TCAD models similar to the TCADI models while there is stronger short-
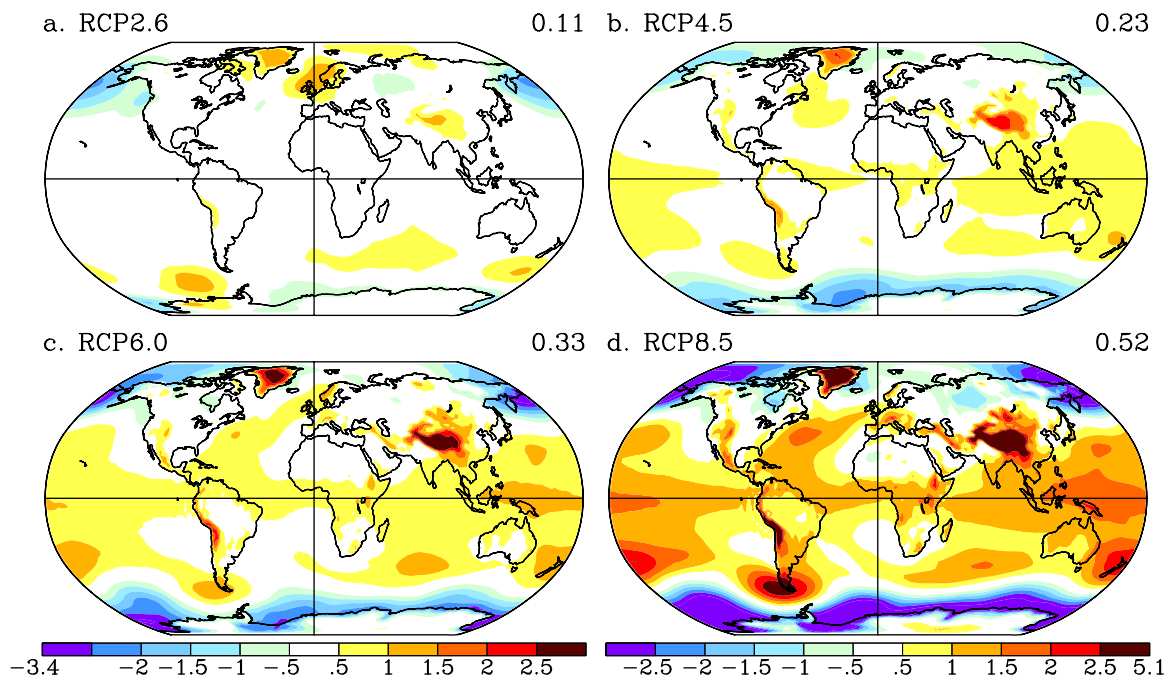
Figure 10. Sea level pressure differences (mb) for late 21st century 2081–2100 minus 1986–2005 of the corresponding historical ensemble member for the NINT climate model. (a) RCP2.6; (b) RCP4.5; (c) RCP6.0; and (d) RCP8.5.
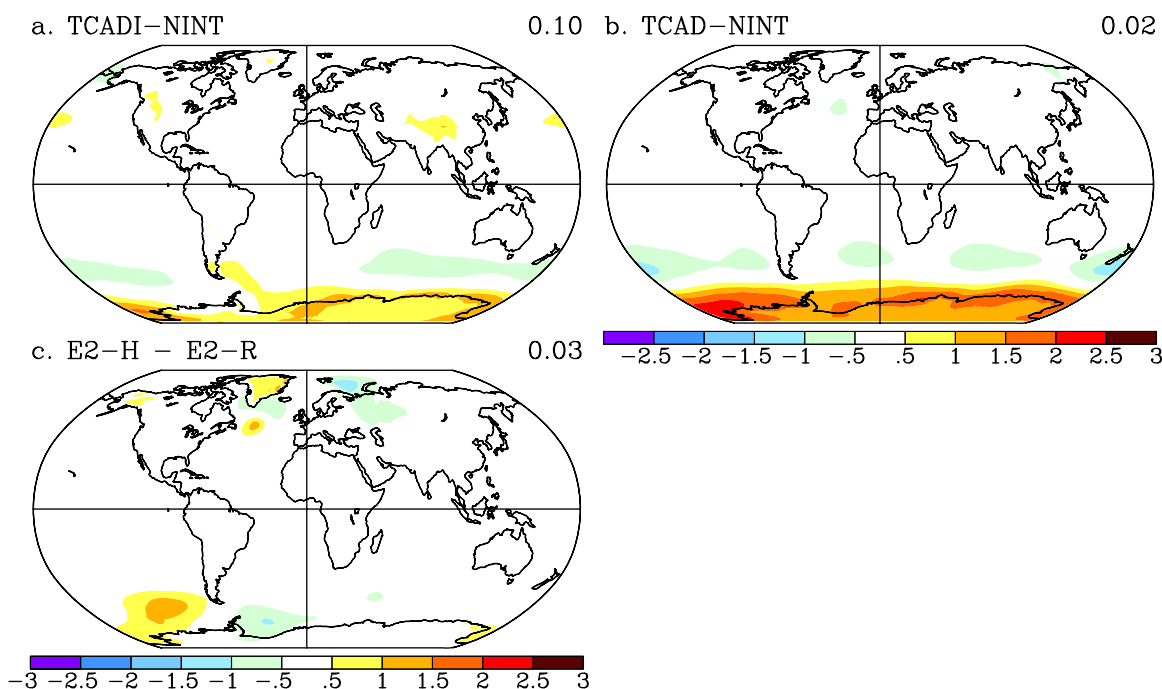
Figure 11. Differences of sea level pressure change (mb) in different climate models for the RCP4.5 scenario. (a) TCADI-NINT; (b) TCAD-NINT; and (c) E2-H minus E2-R.

wave radiative heating due to reduced cloud cover over the polluted land areas, such as southern regions in China, North America, and Northern Europe in the NINT models (Figure 14b).

The larger sea ice reduction off the east coast of Greenland follows stronger warming in the E2-H models (Figure 7c), which in turn lead to a greater low and total cloud cover reduction (Figure 13c) and to a corresponding increase in the short-wave radiative flux (Figure 14c). The contrasting surface cooling to the south of Greenland in the E2-H models (Figure 7c) is a result of reduced North Atlantic overturning circulation in all warming scenarios (discussed in the next section). This leads to low and total cloud cover increases in the E2-H models (Figure 13c) and to corresponding decreases in the short-wave and total cloud radiative forcing compared to the E2-R models (Figure 14c). Higher resolution of the ocean equatorial waveguide in the E2-H model is associated with contrasting cloud cover changes and respective cloud short-wave and total cloud radiative forcing over tropical Pacific Ocean and Southern Ocean.

6. Projections of Future Climate Change Beyond the 21st Century

The global energy disequilibrium ranges between 0.5 and 1.3 W m^{-2} at the end of historical simulation at the year 2005 (Figure 4). In RCP2.6, the climate system slowly gets to equilibrium by the year 2500. In both RCP4.5 and RCP6.0, the energy imbalances decreased after the radiative forcings are kept constant at the year 2150 values and there is still a disequilibrium between 0.1 and 0.8 W m^{-2} and between 0.4 and 0.9 W m^{-2} at the year 2500, respectively. The maximum energy disequilibrium between 2.5 and 2.9 W m^{-2} in the strongest warming scenario RCP8.5 is reached at the end of the 21st century. Then there is a gradual decline of energy imbalance, but it remains large and positive (1.2–1.5 W m^{-2}) at the year 2500. Temperatures continue to increase for all scenarios while the imbalance is positive (Table 1).

In RCP2.6, there are recoveries of the globally averaged surface air temperature for all versions of the GISS climate model reflecting a slow decrease of greenhouse gas concentrations from the middle of the 21st century. In the RCP2.6 scenario, the climate cools at the end 25th century relative to the year 2100 with the NINT and TCAD configurations. Both TCADI E2-R and E2-H show stronger warming by the year 2050 compared to both TCAD and NINT versions and then much slower surface temperature recovery over 450 years in the RCP2.6 experiment (the fifth and sixth rows in Table 1). Figure 3, which summarizes the surface air temperature change for all coupled model configurations, shows the temperature recovery in the RCP2.6
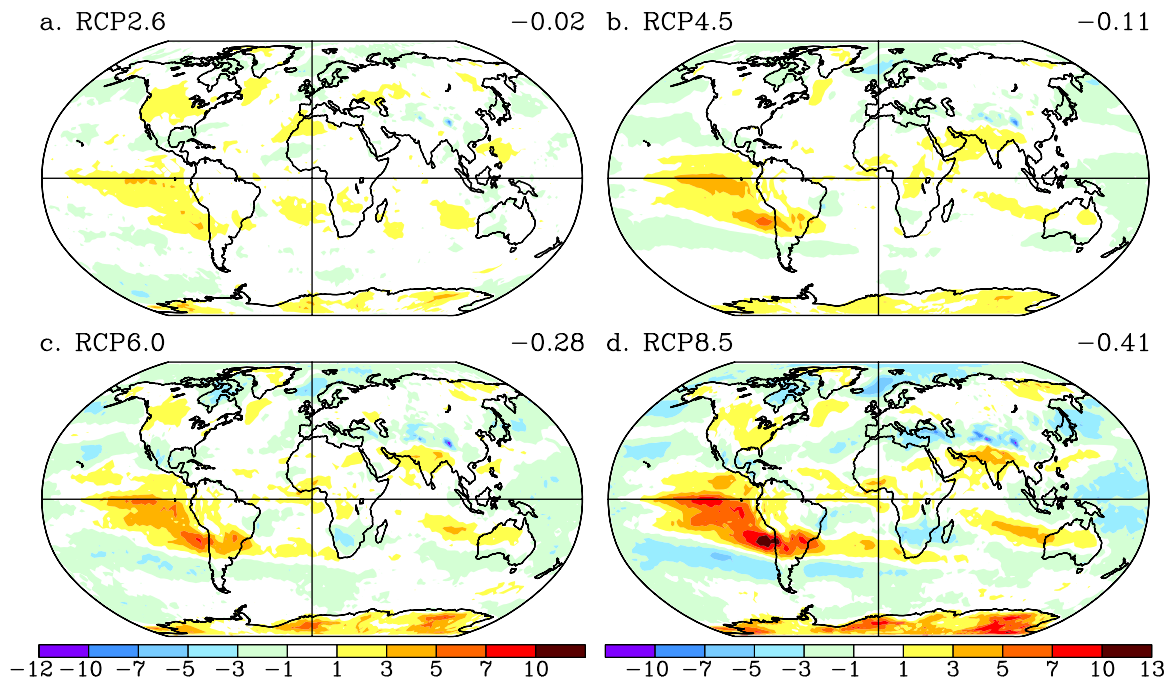
Figure 12. Total cloud cover differences (%) for late 21st century 2081–2100 minus 1986–2005 of the corresponding historical ensemble member for the NINT climate model. (a) RCP2.6; (b) RCP4.5; (c) RCP6.0; and (d) RCP8.5.

scenario to the value of the end of the historical simulations. For the period 2101–2500, there is downward trend $-0.13°C$/century that leads to a recovery of the surface air temperature to the preindustrial state. However, the thermosteric contribution to sea level rise continues to increase through 2500 even though temperatures return to twentieth century values. Continental ice sheets may also continue to melt despite this temperature recovery.
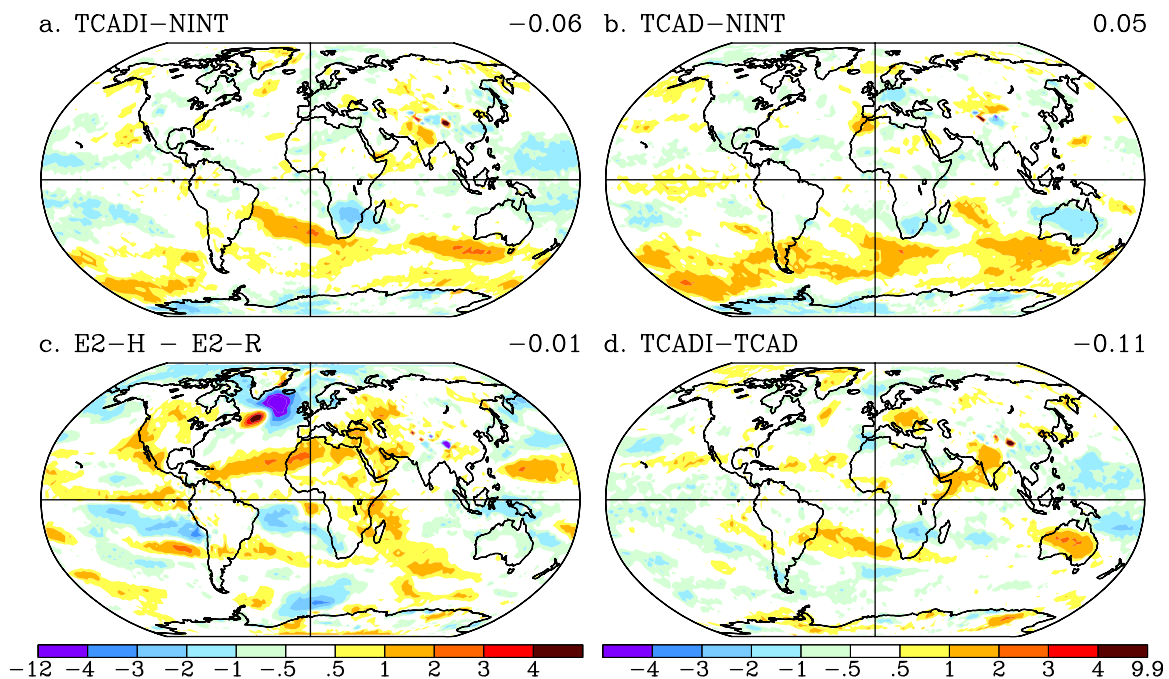
Figure 13. Differences of total cloud cover change (%) in different climate models for the RCP4.5 scenario. (a) NINT-TCAD; (b) NINT-TCADI; (c) E2-H minus E2-R; and (d) TCAD-TCADI.
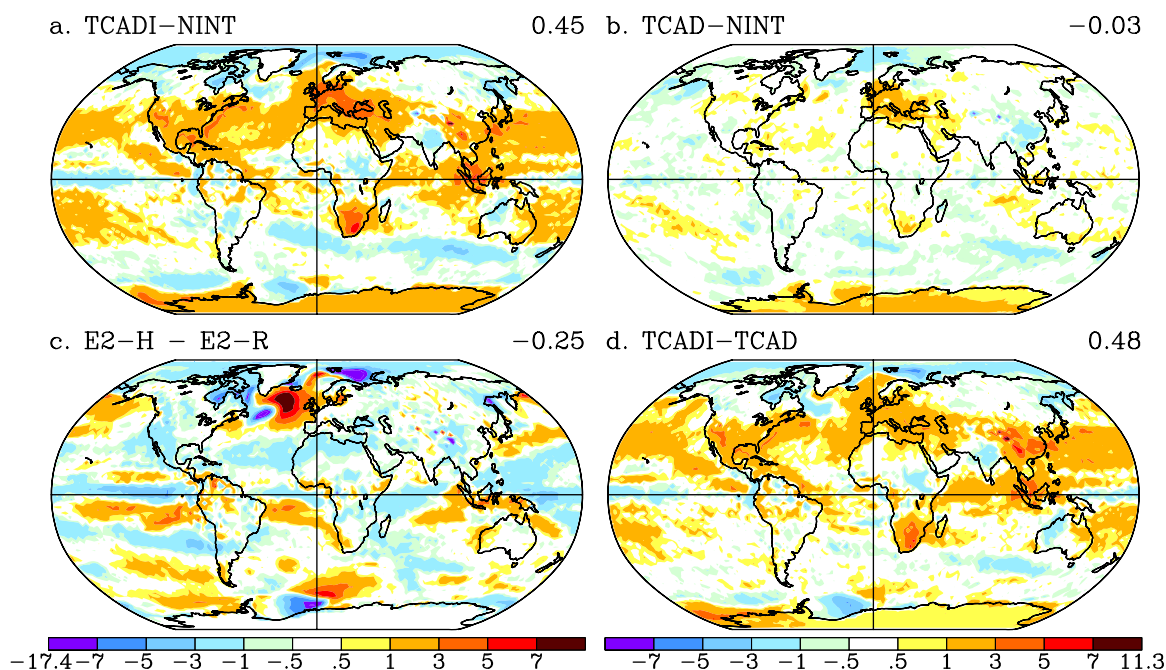
Figure 14. Differences of short-wave cloud radiative forcing (W m²) in different climate models for the RCP4.5 scenario. (a) NINT-TCAD; (b) NINT-TCADI; (c) E2-H minus E2-R; and (d) TCAD-TCADI.

Beyond the 21st century, the Earth's surface continues to warm in all models in the RCP6.0 and RCP8.5 experiments. The temperature increase ranges between 2.6 and 3.5°C by the end of the 25th century in the RCP6.0 experiment and between 5.3 and 6.4°C in the RCP8.5 scenario. The positive linear trend of the surface temperature is 0.13°C/century from the year 2001–2500 in the RCP4.5 case while the positive linear trends are stronger for RCP6.0 and RCP8.5 scenarios reaching 0.2 and 0.5°C/century, respectively. The thermal ocean expansions are the largest of 115–131 cm for RCP8.5 at the year 2300 relative to (1996–2005) mean sea level of the historical simulation while smaller thermosteric sea level rises are reproduced on other RCP scenarios (Table 3).

The E2-R climate models show much stronger decline of the North Atlantic overturning (Figure 15a) compared to E2-H models (Figure 15b). By 2500, the E2-R RCP8.5 experiments show a complete collapse of the overturning stream function while the E2-H RCP8.5 cases maintain 35–40% of the present-day North Atlantic overturning after the year 2200.

The overturning stream function recovers completely by the year 2400 in RCP4.5 and partially in RCP6.0 experiments with E2-R NINT and TCAD models. In case RCP6.0 with greater warming, there are smaller areas (compared to the scenario RCP4.5) of deep water formation in the North Atlantic which maintain the convection and partial recovery of the overturning stream function the E2-R NINT and TCAD models. The E2-R TCADI model behaves differently and does not show any recovery in RCP4.5 and RCP6.0. Due to different climatic conditions, such as cloudier and rainier (Figures 13a and 13d) conditions, surface buoyancy forcings with cooler and less salty surface ocean layer in the North Atlantic lead to an equilibrium state of the overturning circulation without strong deep water formation in the E2-R TCADI models. The North Atlantic overturning circulation equilibrates at about 60% in the RCP4.5 and at about 55% in the RCP6.0 relative to the control simulation with 1850 climate conditions.

In RCP8.5, all configurations of the E2-R climate model produce the complete shutdown of the convection and deep water formation in the North Atlantic by 2300. Due to large sea ice melting in the Arctic, the top ocean layer becomes very fresh in all E2-R RCP8.5. Reduction of the northward transport of warm tropical Atlantic waters leads to a colder surface layer in the regions of convection in the North Atlantic. The fresh and cold ocean surface causes strong stratification without deep water formation.

The E2-H model overturning circulation does not recover in either the RCP4.5 or RCP6.0 scenarios for any atmospheric model configurations. In fact, for all configurations the E2-H models produce about the same
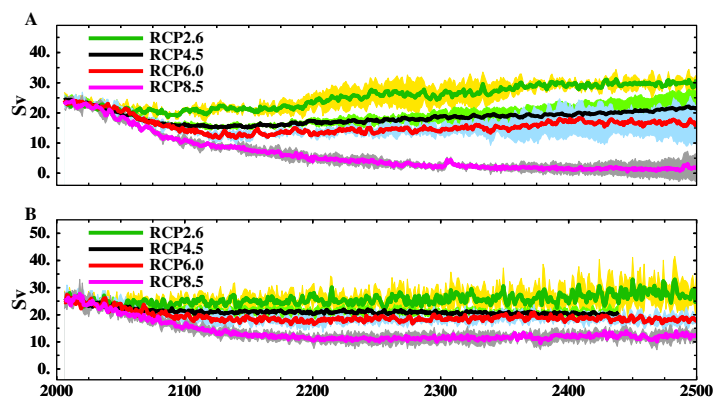
Figure 15. North Atlantic overturning stream function (Sverdrup). Different shadings indicate ranges of the RCP experiments with the NINT, TCAD, and TCADI climate models. (a) E2-R; (b) E2-H.

slowdown in Atlantic overturning with 35–40% reduction in the RCP4.5 scenario and about 40–45% reduction in RCP6.0 (Figure 15b). After such reductions, the overturning circulations are fairly steady without strong North Atlantic deep water formation. This equilibrium state of reduced Atlantic overturning in E2-H models is stabilized by increased surface temperatures and salinities in the North Atlantic. There is a negative feedback between the increased salinities and maintaining the convective processes and overturning in the North Atlantic in the E2-H climate models. Even in the scenario with the strongest warming RCP8.5, the Atlantic overturning stream function reaches the equilibrium state of 35–40% of the control simulation.

In the RCP2.6 scenario, all atmospheric configurations of both coupled models E2-R and E2-H show complete recovery of the Atlantic overturning stream function by the year 2500 (Figure 15). The recovery of the Atlantic overturning follows the recovery of the climate system to the state of the late twentieth century (Figures 3 and 4).

In summary, Figure 16 presents the sensitivity of the North Atlantic meridional overturning circulations to the change of the global annual mean surface air temperature for each RCP experiment and all coupled model configurations. The changes of both the North Atlantic overturning and surface air temperature are taken for the late 25th century 2481–2500 minus 1986–2005. The correlation and dependence of the overturning on surface air temperature are stronger in the climate models E2-R compared to E2-H (blue symbols and blue linear trend line for E2-R versus red symbols and red linear trend line for E2-H). The fast weakening of the North Atlantic overturning due to strong warming and excessive sea ice melting in the E2-R models leads to complete shutdown of convective processes and deep water formation. In the E2-H models the meridional overturning remains half the overturning strength of the control simulation in the RCP8.5 experiments with the largest warming.

7. Normalized Response

Another way to show the geographical patterns of warming and precipitation is considering patterns of change scaled to 1°C global mean surface temperature change. Such a normalization factors out the effects that are directly related to climate sensitivity. Instead it shows the regional differences simulated by different models as well as changes in regional responses in different RCP scenarios.

Figure 17a shows the surface air temperature change averaged over the last two decades of simulations, 2481–2500, relative to the correspondent historical simulation for 1986–2005, normalized by the change in the annual global mean surface temperature for the NINT E2-R climate model in the scenario RCP4.5. Although the warming patterns are very similar for different configurations of GISS climate model, there are some differences such as stronger Arctic amplification in the E2-H model (Figure 17b) due to greater warming (Figure 7c) and more extensive sea ice melt in the high northern latitudes. Figure 17c shows contrasting temperature change over the northern and southern Atlantic Ocean in the RCP8.5 compared to the scenario RCP4.5. There is less warming over the North Atlantic in the RCP8.5 case because there is much smaller ocean heat transport from low tropical latitudes to the north in the RCP8.5. This keeps the tropics and southern Atlantic temperature warmer compared to the temperatures over the North Atlantic. The dipole warming/cooling over the Atlantic/Pacific equatorial ocean regions in the E2-H models (Figures 7c and 17b) is a reflection of stronger El Nino variability in this model which is also clearly presented in the sea level pressure variability.
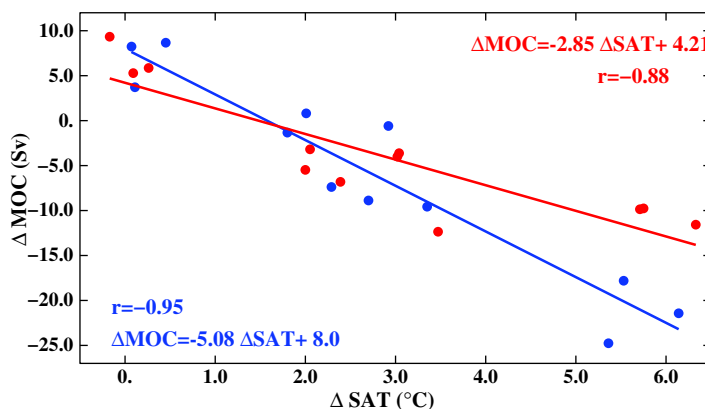
Figure 16. Relationship between the surface air temperature difference and the North Atlantic meridional overturning circulation for the late 25th century 2481–2500 minus 1986–2005. The blue symbols are for RCP experiments with different configurations of E2-R model; the red symbols are for the E2-H models.

The CMIP5 multimodel global mean precipitation increase in the transient CO_2 increase experiment corresponds to 1.4% [*Pendergrass and Hartmann*, 2014]. NINT E2-R is in the middle on the CMIP5 models. The most of the precipitation changes can be explained by the global warming that is presented in Figure 18a. There is the enhancement of precipitation over the intertropical convergence zone, over the North Pacific and Southern Ocean. The shift of the increased precipitation to the south from the equator and the reduced precipitation to the north from the equator over the Atlantic Ocean (Figure 18c) follows the pattern of the temperature change in the case RCP8.5. The reduced precipitation along the equator in the E2-H climate model (Figure 18b) needs more investigation. The pattern of increased and decreased precipitation over the northern North Atlantic in the E2-H (Figure 18b) is in accord with temperature change in this model.

8. Conclusions

The simulations described here show projected climate responses to a wide range of 21st century anthropogenic forcing scenarios and their extensions to 2500. To a large extent the results are unsurprising: the greater the future forcing, the greater the warming and larger the impacts on other components of the climate system. However, the variety of scenarios used, from high mitigation to business-as-usual, allows us to quantify the resulting climate response, identify physical quantities that do not respond linearly, and assess where rates of change (as opposed to the change itself) appear to be important. Additionally, our exploration of dependence of the response to the ocean model or interactive composition allows us to probe (in a limited way) the structural uncertainties in our projections.

We have shown results for the time period 2006–2500. Full equilibrium response of the climate system occurs over millennia, mainly due to ocean thermal inertia [*Hansen et al.*, 1985]. However, in the real world there are factors that are missing in the models that would inevitably come into play. Changes of vegetation—both in composition and response of specific plant functional types—will change the surface response. Impacts of warming on ice sheets will impact their albedo, shape, extent, and contributions to sea level rise beyond the thermosteric effects quantified here. Other composition-related feedbacks are also not included, for instance, permafrost degradation and its impacts on the high-latitude carbon and methane cycles and changes in ocean marine biogeochemical cycles (via changes in surface albedo, carbon cycling, dimethyl sulfide (DMS) and methane sulfonic acid (MSA) emissions). Therefore, given the positive sign and significant magnitude of slow Earth system-feedbacks inferred from Cenozoic climate change [*Hansen et al.*, 2008] or the Pliocene [*Lunt et al.*, 2010], the long-term results in these simulations should be seen as lower bounds for the multicentury and longer time scales.

There are some consistent patterns across our ensemble: the TCADI coupled models with the interactive aerosol chemistry and indirect aerosol effect show the largest warming compared to the two other models. The E2-H coupled models produce warmer surface air temperatures in the most cases due to reduced rates of ocean heat uptake relative to the E2-R configurations.

The high-mitigation scenario RCP2.6 is the only one that limits global warming to below the widely discussed 2°C threshold at the end of the 21st century relative to the preindustrial surface temperature. However, even in this scenario, the thermosteric contribution to sea level rise continues to increase through 2500 even though temperatures return to twentieth century values. Continental ice sheets will likely also
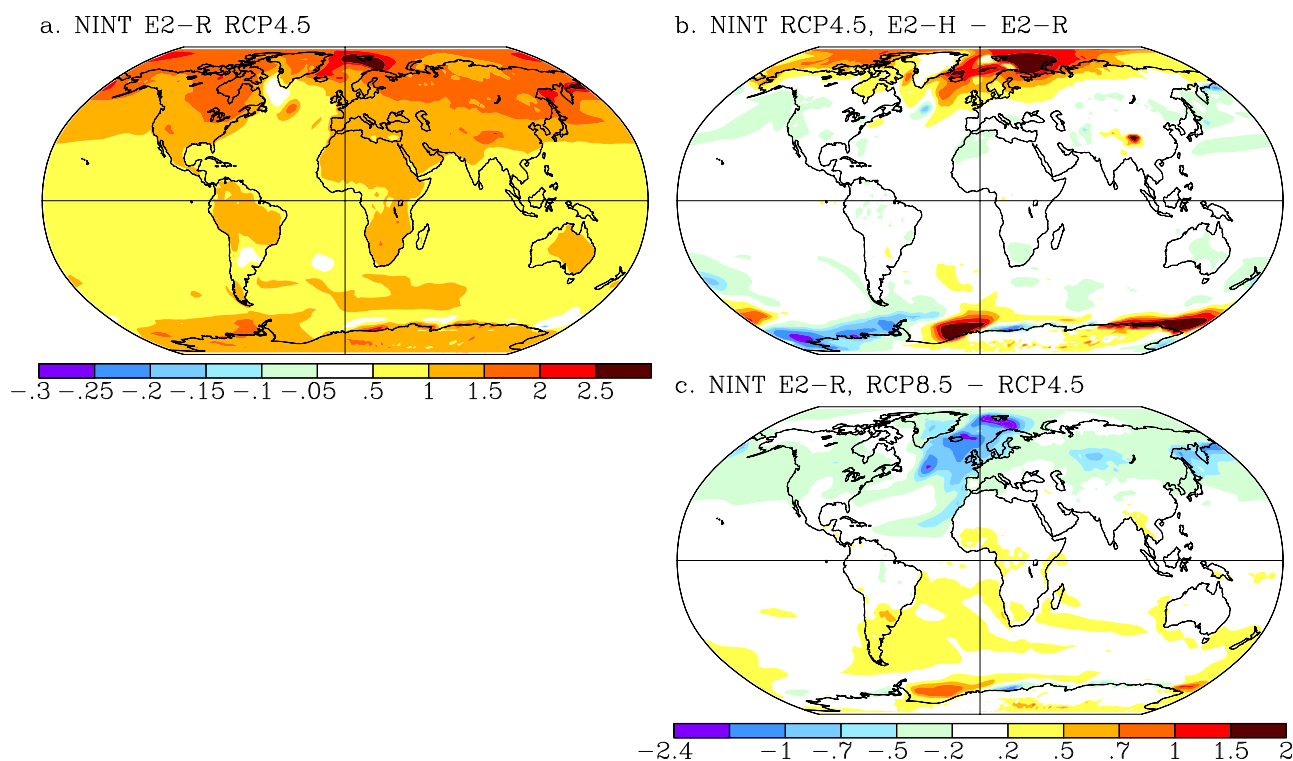
Figure 17. Normalized surface air temperature change for late 25th century 2481–2500 minus 1986–2005 of the corresponding historical ensemble member of the climate model by the change in annual global mean surface temperature. (a) NINT RCP4.5, E2-H–E2-R; (b) NINT E2-R RCP4.5; and (c) NINT E2-R, RCP8.5-RCP4.5.

continue to melt despite this temperature recovery. Two E2-R models, NINT and TCAD, show the recovery of the Northern Hemisphere annual mean sea ice cover (3–4% above the minimum extent values). By contrast, the E2-R TCADI model has a 7.6% decrease (from 2006) reflecting the much stronger warming in this model compared to the other two. The surface air temperature increase is larger in the E2-H models during the historical simulations of the twentieth century, which is accompanied by too little sea ice coverage. This leads to a strong negative ice bias and a nearly ice-free Arctic summer within two decades of the present in all RCP experiments.

Despite the missing processes noted above, future projections provide valuable information in climate understanding. The fact that the GISS climate model can reproduce the current climate and the recent observed trends provides support for model credibility, at least for global mean and large-scale variables. The value of climate projections is increased when multiple models with different levels of complexity are used [*Held*, 2005], and so it is important to determine what processes and parameters are responsible for model disagreements in their projections. For instance, the climate models with interactive chemistry and aerosols compared to the NINT models with prescribed values show the areas where results depend on these model assumptions, such as regions in South Asia, Europe, and North America.

For predictions on shorter time scales, the impacts of internal variability and accurate initial conditions are more important, especially regionally, implying that there are significant limits to the precision of any model projection even if scenarios are perfect [*Deser et al.*, 2012]. The last decade or two provides a salutary example of the importance of unforced variations in tropical climate that are out of phase between the models and observations, variability in ocean heat uptake, and misspecification of climate drivers [e.g., *Kosaka and Xie*, 2013; *Schmidt et al.*, 2014b]. Our near-term results will also suffer from these same deficiencies and so need to be interpreted carefully. For example, the September Arctic ice-free conditions are obtained within 10–15 years due to different initial conditions for each ensemble member in the RCP4.5 that confirms the presence of initial condition uncertainty.

But how seriously should we take these simulations? If we accept the input scenarios as valid for the moment, the magnitude of the structural uncertainty in the medium to long-term response is still unknown.
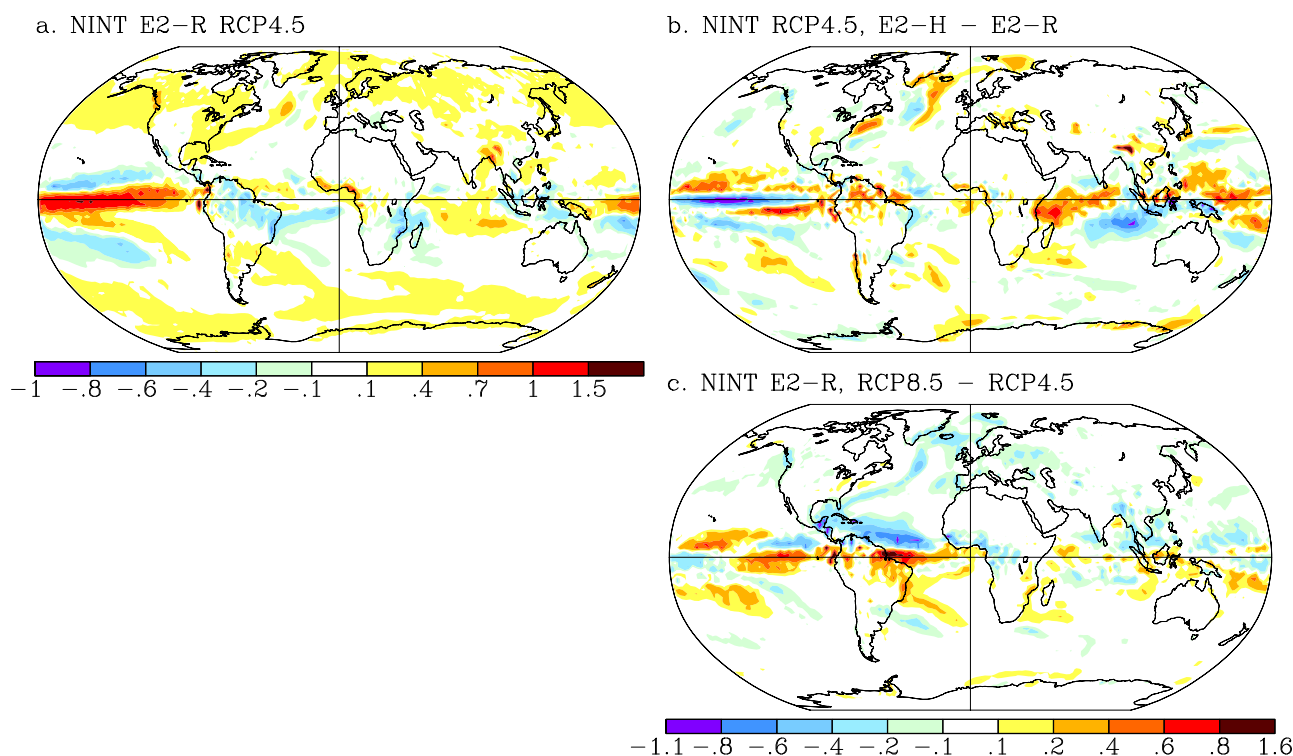
Figure 18. Normalized precipitation change for late 25th century 2481–2500 minus 1986–2005 of the corresponding historical ensemble member of the climate model by the change in annual global mean surface temperature. (a) NINT RCP4.5, E2-H–E2-R; (b) NINT E2-R RCP4.5; and (c) NINT E2-R, RCP8.5-RCP4.5.

The models we describe here include structural variations associated with the ocean model component and the interactivity of the atmospheric composition. In these simulations, the impact of varying the ocean model is significantly larger than the importance of the interactivity of the atmospheric composition. For example, the equilibrium state of the Atlantic meridional overturning circulation is completely different between the two ocean models in the RCP8.5 scenario.

In the case with the smallest forcing (RCP2.6), the complete recovery of the Atlantic overturning in both climate models E2-R and E2-H follows the recovery of the climate system to the state of the late twentieth century by the year 2500. In RCP4.5 the NINT and TCAD E2-R models show the complete recovery the Atlantic overturning and partial recovery in the RCP6.0 while the overturning circulation collapses in the RCP8.5 scenario in all coupled model E2-R configurations. The E2-H models overturning circulation do not show any recovery in either RCP4.5 or RCP6.0 scenarios. The changes in the Atlantic overturning circulation are closely related to the upper ocean, where the nonlocal salinity feedbacks lead to restoring and keeping the overturning stable in the E2-H models. We conclude that North Atlantic response is a complicated function of time scale, magnitude of forcing, and representation of key ocean processes. Thus, this wide range of responses is a key uncertainty in future climate projections.

There have been attempts to constrain the overturning sensitivity to forcings through the study of paleoclimatic examples of overturning variability [*Schmidt*, 2010], for instance the 8.2 kyr event [*LeGrande et al.*, 2006; *Schmidt and LeGrande*, 2005]. A more coherent testing of models against paleoclimate targets may well be the best strategy to reduce structural uncertainty, since we only have 10 years of direct observations of the Atlantic overturning, a time period that is insufficient to constrain multidecadal responses [*Smeed et al.*, 2014].

We have tried to show which elements of the responses to the RCPs are robust across time scale, magnitude of warming, and the structural variations that we explored. For those elements that are robust among the GISS models, it will be interesting to see whether they are also robust across the multimodel ensemble (such as in CMIP5), though it is beyond the scope of this paper to explore this. For the elements that vary greatly across even the GISS ensemble, it should be expected that there will be similar (or greater) variation

across CMIP5 and it is these aspects that will benefit most from well-designed tests using paleodata to discriminate between behaviors [*Collins et al.*, 2013].

References

Andrews, T., J. M. Gregory, M. J. Webb, and K. E. Taylor (2012), Forcing, feed-backs and climate sensitivity in CMIP5 coupled atmosphere-ocean climate models, *Geophys. Res. Lett.*, *39*, L09712, doi:10.1029/2012GL051607.

Bleck, R. (2006), An oceanic general circulation model framed in hybrid isopycnic-cartesian coordinates, *Ocean Modell.*, *4*, 55–88.

Bond, T., D. Streets, K. Yarber, S. Nelson, J.-H. Wo, and Z. Klimont (2004), A technology-based global inventory of black and organic carbon emissions from combustion, *J. Geophys. Res.*, *109*, D14203, doi:10.1029/2003JD003697.

Bony, S., and J.-L. Dufresne (2005), Marine boundary layer clouds at the heart of tropical cloud feedback uncertainties in climate models, *Geophys. Res. Lett.*, *32*, L20806, doi:10.1029/2005GL023851.

Brient, F., and S. Bony (2013), Interpretation of the positive low-cloud feedback predicted by a climate model under global warming, *Clim. Dyn.*, *40*, 2415–2431, doi:10.1007/s00382-011-1279-7.

Church, J. A., N. J. White, L. F. Konikow, C. M. Domingues, J. G. Cogley, E. Rignot, J. M. Gregory, M. R. van den Broeke, A. J. Monaghan, and I. Velicogna (2011), Revisiting the Earth's sea-level and energy budgets from 1961 to 2008, *Geophys. Res. Lett.*, *38*, L18601, doi:10.1029/2011GL048794.

Clement, A. C., R. Burgman, and J. R. Norris (2009), Observational and model evidence for positive low-level cloud feedback, *Science*, *325*(5939), 460–464, doi:101126/science.1171255.

Dai, A., T. M. L. Wigley, B. A. Boville, J. T. Kiehl, and L. E. Buja (2001), Climates of the twentieth and twenty-first centuries simulated by the NCAR climate system model, *J. Clim.*, *14*, 485–519.

Del Genio, A. D., W. Kovari, M. S. Yao, and J. Jonas (2005), Cumulus microphysics and climate sensitivity, *J. Clim.*, *18*, 2376–2387.

Deser, C., R. Knutti, S. Solomon, and A. S. Phillips (2012), Communication of the role of natural variability in future North American climate, *Nat. Clim. Change*, *11*, 775–779, doi:10.1038/nclimate1562.

Dunne, J. P., et al. (2012), GFDL's ESM2 global coupled climate-carbon Earth System Models. Part I: Physical formulation and baseline simulation characteristics, *J. Clim.*, *25*, 6646–6665, doi:10.1175/JCLI-D-11–00560.1.

Gent, P. R., and J. C. McWilliams (1990), Isopycnal mixing in ocean circulation models, *J. Phys. Oceanogr.*, *20*, 150–155.

Giorgetta, M., et al. (2013), Climate and carbon cycle changes from 1850 to 2100 in MPI-ESM simulations for the Coupled Model Intercomparison Project phase 5, *J. Adv. Model. Earth Syst.*, *5*, 572–597, doi:10.1002/jame.20038.

Hallberg, R., A. Adcroft, J. Dunne, J. Krasting, and R. Stouffer (2013), Sensitivity of 21st century global-mean steric sea level rise to ocean model formulation, *J. Clim.*, *26*, 2947–2956, doi:10.1175/JCLI-D-12–00506.1.

Hansen, J., and M. Sato (2004), Greenhouse gas growth rates, *Proc. Natl. Acad. Sci. U. S. A.*, *101*, 16,109–16,114.

Hansen, J., Russell, G., Lacis, A., I. Fung, D. Ring, and P. Stone (1985), Climate response times: Dependence on climate sensitivity and ocean mixing, *Science*, *229*, 857–859.

Hansen, J., et al. (2005a), Efficacy of climate forcings, *J. Geophys. Res.*, *110*, D18104, doi:10.1029/2005JD005776.

Hansen, J., et al. (2005b), Earth's energy imbalance: Confirmation and implications, *Science*, *308*, 1431–1435, doi:10.1126/science.1110252.

Hansen, J., et al. (2007), Dangerous human-made interference with climate: A GISS modelE study, *Atmos. Chem. Phys.*, *7*, 2287–2312, doi:10.5194/acp-7–2287-2007.

Hansen, J., M. Sato, P. Kharecha, D. Beerling, R. Berner, V. Masson-Delmotte, M. Pagani, M. Raymo, D. L. Royer, and J. C. Zachos (2008), Target atmospheric CO_2: Where should humanity aim? *Open Atmos. Sci. J.*, *2*, 217–231, doi:10.2174/1874282300802010217.

Hawkins, E., and R. Sutton (2009), The potential to narrow uncertainty in regional climate predictions, *Bull. Am. Meteorol. Soc.*, *90*, 1095–1107, doi:10.1175/2009BAMS2607.

Hegerl, G. C., et al. (2007), Understanding and attributing climate change, in *Climate Change 2007: The Physical Science Basis*, edited by S. Solomon et al., pp. 663–745, Cambridge Univ. Press, Cambridge, U. K.

Held, I. M. (2005), The gap between simulation and understanding in climate modeling, *Bull. Am. Meteorol. Soc.*, *86*, 1609–1614.

Held, I. M., and B. J. Soden (2006), Robust responses of the hydrological cycle to global warming, *J. Clim.*, *19*(21), 5686–5699.

Ramaswamy, V., et al. (2001), Radiative forcing of climate change, in *Climate Change 2001: The Scientific Basis. Contribution of Working Group I to the Third Assessment Report of the Intergovernmental Panel on Climate Change*, edited by J. T. Houghton et al., pp. 349–416, Cambridge Univ. Press, Cambridge, U. K.

Collins, M., et al. (2013), Long-term climate change: Projections, commitments and irreversibility, in *Climate Change 2013: The Physical Science Basis. Contribution of Working Group I to the Fifth Assessment Report of the Intergovernmental Panel on Climate Change*, edited by T. F. Stocker et al., pp. 1029–1136, Cambridge Univ. Press, Cambridge, U. K.

Knutti, R., and L. Tomassini (2008), Constraints on the transient climate response from observed global temperature and ocean heat uptake, *Geophys. Res. Lett.*, *35*, L09701, doi:10.1029/2007GL032904.

Koch, D., et al. (2011), Coupled aerosol-chemistry-climate twentieth century model investigation: Trends in short-lived species and climate response, *J. Clim.*, *24*, 2693–2714, doi:10.1175/2011JCl3582.1.

Kosaka, Y., and S.-P. Xie (2013), Resent global-warming hiatus tied to equatorial Pacific surface cooling, *Nature*, *501*, 403–407, doi:10.1038/nature12534.

Large, W. G., J. C. McWilliams, and S. C. Doney (1994), Oceanic vertical mixing: A review and a model with a nonlocal boundary layer parameterization, *Rev. Geophys.*, *32*, 363–403.

LeGrande, A. N., G. A. Schmidt, D. T. Shindell, C. V. Field, R. L. Miller, D. M. Koch, G. Faluvegi, and G. Hoffmann (2006), Consistent simulations of multiple proxy responses to an abrupt climate change event, *Proc. Natl. Acad. Sci. U. S. A.*, *103*, 837–842, doi:10.1073pnas.0510095103.

Lewis, N., and J. A. Curry (2014), The implications for climate sensitivity of AR5 forcing and heat uptake estimates, *Clim. Dyn.*, doi:10.1007/s00382-014-2342-y, in press.

Lunt, D. J., A. M. Haywood, G. A. Schmidt, U. Salzmann, P. Valdes, and H. J. Dowsett (2010), Earth system sensitivity inferred from Pliocene modelling and data, *Nat. Geosci.*, *3*, 60–64, doi:10.1038/NGEO706.

Massonnet, F., T. Fichefet, H. Goosse, C. M. Bitz, G. Philippon-Berthier, M. M. Holland, and P.-Y. Barriat (2012), Constraining projections of summer Arctic sea ice, *Cryosphere*, *6*, 1383–1394, doi:10.5194/tc-6–1383-2012.

Masui, T., K. Matsumoto, Y. Hijioka, T. Kinoshita, T. Nozawa, S. Ishiwatari, E. Kato, P. R. Shukla, Y. Yamagata, and M. Kainuma (2011), An emission pathway for stabilization at 6 Wm^{-2} radiative forcing, *Clim. Change*, *109*, 59–76, doi:10.1007/s10584-011-0150-5.

Meehl, G. A., W. M. Washington, W. D. Collins, J. M. Arblaster, A. Hu, L. E. Buja, W. G. Strand, and H. Teng (2005), How much more global warming and sea level rise, *Science*, *307*, 1769–1772, doi:10.1126/science.1106663.

Meehl, G. A., et al. (2007), Global climate projections, in *Climate Change 2007: The Physical Science Basis. Contribution of Working Group I to the Fourth Assessment Report of the Intergovernmental Panel on Climate Change*, edited by S. Solomon et al., pp. 749–845, Cambridge Univ. Press, Cambridge, U. K.

Meehl, G. A., et al. (2012), Climate system response to external forcings and climate change projections in CCSM4, *J. Clim.*, *19*, 3661–3683.

Meinshausen, M., N. Meinshuasen, W. Hare, S. C. Raper, K. Frieler, R. Knutti, D. J. Frame, and M. R. Allen (2009), Greenhouse emission targets for limiting global warming to $+2°C$, *Nature*, *458*, 1158–1163.

Menon, S., D. Koch, G. Beig, S. Sahu, J. Fasullo, and D. Orlikowski (2010), Black carbon aerosols and the third polar ice cap, *Atmos. Chem. Phys.*, *10*, 4559–4571, doi:10.5194/acp-10-4559-2010.

Miller, R. L., G. A. Schmidt, and D. T. Shindell (2006), Forced annular variations in the 20th century Intergovernmental Panel on Climate Change Fourth Assessment Report models, *J. Geophys. Res.*, *111*, D18101, doi:10.1029/2005JD006323.

Miller, R. L., et al. (2014), CMIP5 historical simulations (1850–2012) with GISS ModelE2, *J. Adv. Model. Earth Syst.*, *6*, 441–477, doi:10.1002/2013MS000266.

Nazarenko, L., N. Tausnev, and J. Hansen (2006), Sea-ice and North Atlantic climate response to CO_2-induced warming and cooling conditions, *J. Glaciol.*, *52*, 433–439.

Nazarenko, L., N. Tausnev, and J. Hansen (2007), The North Atlantic thermohaline circulation simulated by the GISS climate model during 1970-99, *Atmos. Ocean*, *45*, 81–92, doi:10.3137/ao.450202.

Otto, A., et al. (2013), Energy budget constraints on climate response, *Nat. Geosci.*, *6*, 415–416, doi:10.1038/ngeo1836.

Pendergrass, A. G., and D. L. Hartmann (2014), The atmospheric energy constraint on global-mean precipitation change, *J. Clim.*, *27*, 757–768, doi:10.1175/JCLI-D-13-00163.1.

Riahi, K., S. Rao, V. Krey, C. Cho, V. Chirkov, G. Fisher, G. Kindermann, N. Nakicenovic, and P. Rafaj (2011), RCP8.5: A scenario of comparatively high greenhouse gas emissions, *Clim. Change*, *109*, 33–57, doi:10.1007/s10584-011-0149-y.

Roeckner, E., T. Mauritsen, M. Esch, and R. Brokpf (2012), Impact of melt ponds on Arctic sea ice in past and future climates as simulated by MPI-ESM, *J. Adv. Model. Earth Syst.*, *4*, M00A02, doi:10.1029/2012MS000157.

Russell, G. L., J. R. Miller, and D. H. Rind (1995), A coupled atmosphere-ocean model for transient climate change, *Atmos. Ocean*, *33*, 683–730.

Russell, G. L., J. R. Miller, D. Rind, R. Ruedy, G. Schmidt, and S. Sheth (2000), Comparison of model and observed regional temperature changes during the past 40 years, *J. Geophys. Res.*, *105*, 14,891–14,898.

Schmidt, G. A. (2010), Enhancing the relevance of palaeoclimate model/data comparisons for assessments of future climate change, *J. Quat. Sci.*, *25*, 79–87, doi:10.1002/jqs.1314.

Schmidt, G. A., and A. N. LeGrande (2005), The Goldilocks abrupt climate change event, *Quat. Sci. Rev.*, *24*, 1109–1110, doi:10.1016/j.quascirev.2005.01.015.

Schmidt, G. A., et al. (2006), Present day atmospheric simulations using GISS ModelE: Comparison to in-situ, satellite and reanalysis data, *J. Clim.*, *19*, 153–192.

Schmidt, G. A., et al. (2014a), Configuration and assessment of the Giss ModelE2 contributions to the CMIP5 archive, *J. Adv. Model. Earth Syst.*, *6*, 141–184, doi:10.1002/2013MS000265.

Schmidt, G. A., D. T. Shindell, and K. Tsigaridis (2014b), Reconciling warming trends, *Nat. Geosci.*, *7*, 158–160, doi:10.1038/ngeo2105.

Shindell, D. T., R. L. Miller, G. A. Schmidt, and L. Pandolfo (1999), Simulation of recent northern winter climate trends by greenhouse-gas forcing, *Nature*, *399*, 452–455, doi:10.1038/20905.

Shindell, D., G. Faluvegi, N. Unger, E. Aguilar, G. A. Schmidt, D. M. Koch, S. E. Bauer, and J. R. Miller (2006), Simulations of preindustrial, present-day, and 2100 conditions in the NASA GISS composition and climate model G-PUCCINI, *Atmos. Chem. Phys.*, *6*, 4427–4459.

Shindell, D. T., et al. (2013a), Interactive ozone and methane chemistry in GISS-E2 historical and future climate simulations, *Atmos. Chem. Phys.*, *13*, 2653–2689, doi:10.5194/acp-13-2653-2013.

Shindell, D. T., G. Faluvegi, L. Nazarenko, K. Bowman, J.-F. Lamarque, A. Voulgarakis, G. Schmidt, O. Pechony, and R. Ruedy (2013b), Attribution of historical whole atmosphere ozone forcing, *Nat. Clim. Change*, *3*, 567–670, doi:10.1038/nclimate1835.

Smeed, D. A., et al. (2014), Observed decline of the Atlantic meridional overturning circulation 2004–2012, *Ocean Sci.*, *10*, 29–38, doi:10.5194/os-10-29-2014.

Stevens, B., et al. (2013), Atmospheric component of the MPI-M Earth system model: ECHAM6, *J. Adv. Model. Earth Syst.*, *5*, 146–172, doi:10.1002/jame.20015.

Stott, P. A., and C. E. Forest (2007), Ensemble climate predictions using climate models and observational constraints, *Philos. Trans. R. Soc. A*, *365*, 2029–2052.

Stroeve, J., V. Kattsov, A. Barrett, M. Serrese, T. Pavlova, M. Holland, and W. N. Meier (2012a), Trends in Arctic sea ice extent from CMIP5, CMIP3 and observations, *Geophys. Res. Lett.*, *39*, L16502, doi:10.1029/2012GL052676.

Stroeve, J., M. C. Serrese, J. E. Kay, M. M. Holland, W. N. Meier, and A. P. Barrett (2012b), The Arctic's rapidly shrinking sea ice cover: A research synthesis, *Clim. Change*, *110*, 1005–1027, doi:10.1007/s10584-011-0101-1.

Sun, S., and R. Bleck (2006), Multi-century simulations with the coupled GISS-HYCOM climate model: Control experiments, *Clim. Dyn.*, *26*, 407–428, doi:10.1007/s00382-005-0091-7.

Taylor, K. E., R. J. Stouffer, and G. A. Meehl (2012), An overview of the CMIP5 and experiment design, *Bull. Am. Meteorol. Soc.*, *93*, 485–498, doi:10.1175/BAMS-D-11-00094.1.

Thomson, A. M., et al. (2011), RCP4.5: A pathway for stabilization of radiative forcing by 2100, *Clim. Change*, *109*, 77–94, doi:10.1007/s10584-011-0151-4.

Thompson, D. W. J., and J. M. Wallace (1998), The Arctic Oscillation signature in the wintertime geopotential height and temperature fields, *Geophys. Res. Lett.*, *25*, 1297–1300.

Thompson, D. W. J., and J. M. Wallace (2001), Regional climate impacts of the Northern Hemisphere Annular Mode, *Science*, *293*, 85–89.

Twomey, S. (1977), The influence of pollution on the shortwave albedo of clouds, *J. Atmos. Sci.*, *34*(7), 1149–1152.

Van Aardenne, J. A., F. J. Dentener, J. G. J. Olivier, C. G. M. Klein Goldewijk, and J. Lelieveld (2001), A high resolution dataset of historical anthropogenic trace gas emissions for the period 1890–1990, *Global Biogeochem. Cycles*, *15*, 909–928.

van Vuuren, D. P., et al. (2011a), The representative concentration pathways: An overview, *Clim. Change*, *109*, 5–31, doi:10.1007/s10584-011-0148-z.

van Vuuren, D. P., et al. (2011b), RCP2.6: Exploring the possibility to keep global mean temperature increase below 2°C, *Clim. Change*, *109*, 95–116, doi:10.1007/s10584-011-0152-3.

Yao, M.-S., and A. D. Del Genio (1999), Effects of cloud parameterization on the simulation of climate changes in the GISS GCM, *J. Clim.*, *12*, 761–779.

Zhang, J., and D. Rothrock (2000), Modeling Arctic sea ice with an efficient plastic solution, *J. Geophys. Res.*, *105*, 3325–3338.